Numerical simulation of a turbulent channel flow with an acoustic liner

Robin Sebastian[a], David Marx[a,*], Véronique Fortuné[a]

[a] *Institut P' - CNRS - Université de Poitiers - ENSMA*
Site ENSIP - Bât. B17, 6 rue Marcel Doré 86022 Poitiers CEDEX, France

Abstract

Numerical simulations of a compressible turbulent channel flow with an acoustic impedance boundary condition are performed to assess how the flow is modified compared with a channel flow with rigid walls. When the liner resonance frequency is not too large and the resistance sufficiently small, turbulent statistics deviate from those obtained with rigid walls and surface waves are found traveling along the liner surface. For small resonance frequencies these waves are two-dimensional, they have a large wavelength compared to the turbulent structures and modulate these structures. As a result, they transport momentum toward the impedance wall, causing a drag increase. When the resonance frequency increases, the waves along the liner surface progressively lose their spanwise coherence while their streamwise wavelength decreases to get close to the flow typical length scales, which may also result in a drag increase when the resistance is sufficiently small. In the cases in which the surface waves are two-dimensional, a connection is established between them and the unstable modes computed by using a linear stability analysis. Given the streamwise periodicity of the channel, a temporal stability analysis is performed rather than a spatial analysis, the latter being more frequently encountered in acoustic mode computations. This temporal analysis shows that the unstable mode in the vicinity of an acoustic liner arises from the A-branch of wall modes.

Keywords: duct acoustics, acoustic liner, numerical simulation, instability, turbulence, channel flow
PACS: 43.28.Py, 43.20.Mv, 47.27.nd

1. Introduction

Perforate acoustic liners are an important technology to absorb sound in ducts such as turbofan engines or to suppress combustion instabilities. In many practical situations, the liners are subject to high velocity flows and turbulence, and much research has been devoted to the effect of a grazing flow on the liner impedance. It is for example well known that the resistance tends to increase linearly with the grazing flow speed whereas the reactance tends to decrease [1, 2, 3] as a result of the interaction between the acoustic and vortical

*Corresponding author

Email address: david.marx@univ-poitiers.fr (David Marx)

modes in the holes of the perforated face sheet. Conversely, the liner may modify the flow and turbulence in its vicinity, compared with a rigid wall. An effect of this is a drag increase [4], especially for large liner porosity. Another effect is the flow instability observed in the vicinity of a low resistance liner [5].

Several numerical simulations in flow ducts with liners have been performed in connection with this topic. The objective of many simulations has been to study sound propagation in lined ducts with a known base flow using the linearized Euler or Navier-Stokes equations. A difficulty is then to impose a well-posed impedance boundary condition, especially in time-domain solvers [6, 7, 8, 9, 10, 11, 12, 13, 14, 15, 16]. These simulations neglect both the effect of the grazing flow on the impedance and the effect of the impedance on the flow. Other simulations are based on the full nonlinear Navier-Stokes equations and the flow is computed together with the acoustic field [17, 18, 19, 20, 21, 22]. Among these simulations, some include the liner back cavity and the face sheet perforations [17, 18, 19, 20] so as to include all possible flow-acoustics interactions. Others use an impedance boundary condition with a given impedance [21, 22, 23], which means that the effect of the flow on the impedance is no part of the computation. Jimenez et al (2001) compute a turbulent incompressible channel flow above a purely resistive porous surface [23]. They observed modified turbulent statistics over the surface compared with a rigid wall, and part of this change was associated with spanwise coherent structures moving along the wall. This observation was partly confirmed by a linear stability analysis, unstable modes being present for low values of the resistance. The porous surface being a purely resistive one, resonance mechanisms typically encountered in acoustic liners were not present in this investigation. Olivetti et al. (2015) [21] compute the sound propagation in a lined pipe, a simple model for a nozzle, in order to suppress resonant modes in the duct which have a strong impact on the noise produced by the jet out of the nozzle. Scalo et al. (2015) [22] study the turbulent flow in a compressible periodic channel flow with an impedance boundary condition and describe how the structure of turbulence is modified as the liner resistance decreases. They set the resonance frequency of the liner so that it corresponds to some typical time scale of the flow. As a result the liner resonance frequency is rather high, and larger than typical frequencies encountered in aeroacoustic applications. Compared with Scalo et al. (2015) smaller resonance frequencies will be considered in the present work. More specifically the resonance frequency and other liner parameters are close to those used in the experiments in Marx et al (2010) in which an instability was observed, and for which related linear stability analyses were performed in Marx and Aurégan (2010,2013) [24, 25]. Apart from sound damping in ducts, there is a growing interest in passive methods for aeroacoustics and flow control [26], and a better knowledge of the behavior of the flow in the vicinity of non-rigid wall is useful in general.

This paper makes a new contribution to the investigation of turbulent channel flows with acoustic liners (limited to locally reacting, perforate-like liners).

Numerical Implicit Large Eddy Simulations (ILES) of compressible turbulent channel flows are performed to study what changes in the flow may result from using an impedance boundary condition, in comparison with a rigid wall boundary condition. For some liner parameters, surface waves are computed and their effect on drag is evidenced. A temporal stability analysis complements the simulations and is a useful counterpart to the more classical spatial stability analysis for these waves. The numerical model is presented in Section 2, including the impedance boundary condition, taken to be of the mass-spring-damper type. The different configurations and the corresponding flow statistics are presented in section 3. In particular, the effect of the impedance resonance frequency and resistance on the structures of turbulence is investigated. The surface waves are described in Section 4. In Section 5 it is shown how they can increase the drag on the liner surface. The temporal linear stability analysis is conducted in Section 6. Finally conclusions are given in Section 7.

2. Numerical model

In this section, we introduce the equations of our problem, then present quickly the numerical methods to solve these equations, and finally introduce the model for the impedance boundary condition as well as its numerical implementation.

2.1. The equations

Simulations of channel flows that are periodic in the stream-wise and span-wise directions are performed. The bottom and upper wall are either rigid or modeled as an impedance, with a fixed wall temperature (see Section 2.3 for the boundary conditions). The compressible Navier-Stokes equations are implemented in the particular characteristics-like form presented by Sesterhenn [27] which has also been used in [28] for the direct numerical simulation of compressible channel flows. The Cartesian coordinates are denoted by x, y, z (or by x_1, x_2, x_3) for the stream-wise, wall-normal and span-wise directions. The non-dimensional equations are given by:

$$\frac{\partial u}{\partial t} = -\left(\frac{1}{2}(X^+ - X^-) + Y^u + Z^u\right) + \frac{1}{\mathrm{Re}}\frac{1}{\rho}\frac{\partial \tau_{1j}}{\partial x_j} + F \tag{1}$$

$$\frac{\partial v}{\partial t} = -\left(X^v + \frac{1}{2}(Y^+ - Y^-) + Z^v\right) + \frac{1}{\mathrm{Re}}\frac{1}{\rho}\frac{\partial \tau_{2j}}{\partial x_j} \tag{2}$$

$$\frac{\partial w}{\partial t} = -\left(X^w + Y^w + \frac{1}{2}(Z^+ - Z^-)\right) + \frac{1}{\mathrm{Re}}\frac{1}{\rho}\frac{\partial \tau_{3j}}{\partial x_j} \tag{3}$$

$$\frac{\partial s}{\partial t} = -(X^s + Y^s + Z^s) + \frac{(\gamma-1)}{\gamma}\frac{1}{\mathrm{Re}}\frac{1}{p}\left(\Phi + \frac{1}{\mathrm{Pr}}\nabla\cdot(K_t\nabla T)\right) \tag{4}$$

$$\begin{aligned}\frac{\partial p}{\partial t} = &-\frac{\rho c}{2}\left[(X^+ + X^-) + (Y^+ + Y^-) + (Z^+ + Z^-)\right] \\ &+\frac{1}{\mathrm{Re}}(\gamma-1)\left[\Phi + \frac{1}{\mathrm{Pr}}\nabla\cdot(K_t\nabla T)\right]\end{aligned} \tag{5}$$

where the velocity components along the x, y, and z-directions are denoted by u, v, w (or u_1, u_2, u_3), p is the pressure, ρ the density, s the entropy. c is the sound speed given by $c^2 = \gamma p/\rho$, where γ=1.4 is the ratio of specific heats. The quantities $X^{\pm}$, $Y^{\pm}$, $Z^{\pm}$ are the rates of change of the amplitude of the acoustic waves ; X^s, Y^s, Z^s are related to the entropy wave, and Y^u, Z^u, X^v, Z^v, X^w, Y^w are related to the vorticity wave. They are given by the following relations:

$$X^{\pm} = (u \pm c)\left(\frac{1}{\rho c}\frac{\partial p}{\partial x} \pm \frac{\partial u}{\partial x}\right) \tag{6}$$

$$Y^{\pm} = (v \pm c)\left(\frac{1}{\rho c}\frac{\partial p}{\partial y} \pm \frac{\partial v}{\partial y}\right) \tag{7}$$

$$Z^{\pm} = (w \pm c)\left(\frac{1}{\rho c}\frac{\partial p}{\partial z} \pm \frac{\partial w}{\partial z}\right) \tag{8}$$

$$Y^u = v\frac{\partial u}{\partial y} \qquad Z^u = w\frac{\partial u}{\partial z} \qquad X^v = u\frac{\partial v}{\partial x} \tag{9}$$

$$Z^v = w\frac{\partial v}{\partial z} \qquad X^w = u\frac{\partial w}{\partial x} \qquad Y^w = v\frac{\partial w}{\partial y} \tag{10}$$

$$X^s = u\frac{\partial s}{\partial x} \qquad Y^s = v\frac{\partial s}{\partial y} \qquad Z^s = w\frac{\partial s}{\partial z} \tag{11}$$

The viscous stress tensor is:

$$\tau_{ij} = \mu\left(\partial u_i/\partial x_j + \partial u_j/\partial x_i\right) + \left(\kappa - \frac{2}{3}\mu\right)\left(\partial u_k/\partial x_k\right)\delta_{ij}$$

and $\Phi = \tau_{ij}(\partial u_i/\partial x_j)$ is the viscous dissipation. In addition the state equation is $p = ((\gamma-1)/\gamma)\rho T$ and the thermodynamic relation reads $\rho = p^{1/\gamma}e^{-s}$. The dependence of μ on T is given by the power law: $\mu = T^{0.7}$.

The equations above are normalized using the following reference scales for a channel flow (in the following the tilde $\tilde{\cdot}$ indicates a dimensional quantity): the speed of sound $\tilde{c}_w$ at wall temperature $\tilde{T}_w$ (imposed since an isothermal wall boundary conditions is used), the viscosity $\tilde{\mu}_w$ and thermal conductivity $\tilde{K}_{t,w}$ at the wall temperature, the half-height of the channel $\tilde{H}$, the bulk density $\tilde{\rho}_b$ to be defined below, and the adiabatic specific heat $\tilde{c}_p$=$\gamma\tilde{r}/(\gamma-1)$ with $\tilde{r}$ the gas constant. The thermal conductivity is related to the viscosity through the Prandtl number, $\mathrm{Pr} = \tilde{\mu}_w\tilde{c}_p/\tilde{K}_{t,w}$, and Pr=0.7. The Reynolds number resulting from the previous normalization is $\mathrm{Re} = \tilde{H}\tilde{\rho}_b\tilde{c}_w/\tilde{\mu}_w$.

The bulk density used for normalization is defined by $\tilde{\rho}_b =< \tilde{\rho} >_{xyz}$, where $< \cdot >_{xyz}$ denotes the mean over all spatial directions. The bulk velocity is defined by $\tilde{u}_b =< \tilde{\rho}\tilde{u} >_{xyz} /\tilde{\rho}_b$. As no mass can escape the channel $\tilde{\rho}_b$ is constant, and in normalized form ρ_b=1. The normalized velocity u_b is also forced to keep a constant value, which is ensured by changing dynamically the uniform force F appearing in Eq. (1), as done by [29]. Note that due to normalization, u_b=$\mathcal{M}$ where $\mathcal{M} = \tilde{u}_b/\tilde{c}_w$ is the Mach number based on the bulk velocity and the sound speed at the wall. A non-dimensional number commonly used to specify the operating point of a turbulent channel flow is the bulk Reynolds number defined by:

$$\mathrm{Re}_b = \frac{\tilde{\rho}_b \tilde{H} \tilde{u}_b}{\tilde{\mu}_w} \tag{12}$$

In the following we will prescribe Re_b and $\mathcal{M}$, from which the Reynolds number appearing in the equations can be derived using $\mathrm{Re} = \mathrm{Re}_b/\mathcal{M}$.

Another Reynolds number, to which Re_b may be related by an empirical relationship, is the friction Reynolds number defined by:

$$\mathrm{Re}_\tau = \tilde{\rho}_w \tilde{H} \tilde{u}_\tau / \tilde{\mu}_w \tag{13}$$

where $\tilde{\rho}_w$ is the mean density at the wall, and the friction velocity defined as $\tilde{\mathrm{u}}_\tau = \sqrt{\tilde{\tau}_w/\tilde{\rho}_w}$ is computed from the mean wall shear stress $\tilde{\tau}_w = \tilde{\mu}_w(\partial\tilde{U}/\partial\tilde{y})_w$, where $\tilde{U}$ represents the time-averaged streamwise velocity. Classically the viscous length scale is defined by $\tilde{l}_\tau = \tilde{\mu}_w/(\tilde{\rho}_w\tilde{u}_\tau)$. Quantities scaled with $\tilde{l}_\tau$ and $\tilde{u}_\tau$ are indicated with a superscript + in the following.

2.2. Numerical schemes

With the characteristic formulation (1-5) it would be possible to use upwind schemes [30] in the characteristic directions to introduce some dissipation and stabilize the computation as in [27] and this is indeed what used to be done in this code. In the present work, centered schemes have been prefered as the dissipation is tuned more easily by managing it with the second order derivative. The equations are discretized in a collocated manner and the first derivatives are computed with a 6th order compact scheme (scheme (2.1.7) in [31]) for the central points. For the grid point next to the boundary a centered 4th order compact scheme is used (scheme (2.1.6) in [31] with α=1/4), while at the boundary a 3rd order compact upwind scheme is used (scheme (4.1.3) in [31] with α=2). Since the centered scheme is non-dissipative, the extra dissipation needed to stabilize the computations or serve for ILES is introduced through the diffusive terms with the second-order derivative [32, 33, 34](rather than with the convective terms using the first-order derivative if upwind schemes were used). Specifically the second derivative is a 6th order compact scheme with a 3-9 stencil (Eq. (8) in [34]) for which some coefficients can be freely adjusted to impose the level of dissipation. More details can be found in Sebastian et al. [35]. Finally, the time-advancement relies on a classical fourth-order four-step Runge-Kutta method.

2.3. Impedance boundary condition

2.3.1. Rigid wall boundary condition

For a rigid isothermal wall with u=v=w=0 and T=T_w the boundary conditions to apply have been given by Lechner et al. [28]. At the bottom wall for example, Y^- is a known characteristic flux coming from the interior of the domain, and the reflected characteristic flux Y^+ should be calculated. The situation is reversed at the top wall. Lechner et al. give [28] (adapted to the present notation/normalization):

$$Y^+ = Y^- + 2\frac{1}{\mathrm{Re}}\frac{1}{\rho}\frac{\partial \tau_{2j}}{\partial x_j} \quad \text{(bottom wall)} \qquad Y^- = Y^+ - 2\frac{1}{\mathrm{Re}}\frac{1}{\rho}\frac{\partial \tau_{2j}}{\partial x_j} \quad \text{(top wall)} \tag{14}$$

The isothermal boundary condition is obtained by replacing the pressure and entropy equations at the wall with:

$$\frac{\partial p}{\partial t} = -\frac{p}{2c}(Y^+ + Y^-) \tag{15}$$

$$\frac{\partial s}{\partial t} = \frac{\gamma - 1}{\gamma}\frac{1}{2c}\left(Y^+ + Y^-\right) \tag{16}$$

This now needs to be extended to non-rigid walls.

2.3.2. Mass Spring Damper boundary condition

Generally speaking, an impedance boundary condition is a relation between p and v at a given position at the wall. The impedance (or its inverse, the admittance) is a quantity defined in the frequency domain. Its use in a time-domain solver requires that the impedance be transformed into an impulse response in the time-domain, which is done by an inverse Laplace transform. This is not straightforward, since impedance laws that would appear to be satisfying in the frequency domain may actually not satisfy certain desirable physical properties, which can show up in the time domain in the form of instabilities [36]. These properties are: passivity, causality, and reality, as explained by Rienstra (2006) [10]. In particular, when an impedance has been measured at some given real frequencies, a special care should be exercised when performing the complex continuation of the data so that all the above properties are verified.

Several methods have been proposed to comply with these requirements. Tam and Auriault (1996) [6] have introduced a mass-spring-damper (MSD) equation as a simple liner model that accounts for one resonance frequency. It is directly formulated as a second order equation in v in the time domain, with the p derivative acting as a source (see Eq. (17) below). This equation is solved with the same integration method as the other governing equations, that is, with the same time accuracy. The Laplace transform of this equation provides the admittance of the system, which is also of second order. This admittance has been shown to be causal, passive, and real by Rienstra [10] as long as physical

(positive) values of the parameters are used. Fung and Ju (2000) have advocated the use of the reflection coefficient in place of the impedance/admittance as well as the use of a convolution integral instead of a differential equation [37]. Hence, they also consider the MSD surface, but compute the impulse response corresponding to the reflection coefficient of this type of surface. The cost of computing the integral is reduced by the use of recursive convolution [36]. Recursive convolution has also been used in conjunction with impedance or admittance by Reymen et al [38]. Finally, broadband models of the impedance often rely on partial fraction expansion of either admittance/impedance [40, 39] or reflection coefficient[36] into first and second order systems, each of which satisfies the required properties. The impulse response of these systems can then be plugged into a convolution integral, computed recursively. Recursive convolution involves an integral that is often discretized with a second order method, which reduces the order in time of the code. However, by differentiating this integral it is possible to obtain auxiliary differential equations (ADE), the convolution integral being then obtained from the solutions to the ADE. The advantage is that the ADE are integrated with the same method as the governing equations, and Dragna et al (2015) have shown that the order in time of the code is then maintained [41].

In the present study, the characteristics of the liner are inspired from reference [5] in which an instability occurs around the resonance frequency. Hence, the physics of the interaction of the turbulent flow with a single resonance frequency (corresponding normally to absorption of sound) is of interest here, which justifies the choice of a simple mass-spring-damper model. As discussed above, several implementations are possible. Scalo et al (2015) used the reflection coefficient of the MSD wall together with a convolution integral [22], as recommended by Fung and Ju [36]. Their method was extendend in [44, 42], also for use with the Navier-Stokes equations. An inconvenient is that the order of the time integration method decreases (even if it could possibly be fixed by using ADE). In the present work, in order to retain the order of time integration, the implementation of the differential equation has been privileged. At a bottom wall the MSD model in its differential equation form reads:

$$M\frac{\mathrm{d}^2 v}{\mathrm{d}t^2} + Kv + R\frac{\mathrm{d}v}{\mathrm{d}t} = -\frac{\mathrm{d}p}{\mathrm{d}t} \qquad \text{(bottom wall)} \tag{17}$$

where R is the resistance, M is the mass, and K is the spring constant. These quantities are normalized with $\tilde{\rho}_b\tilde{c}_w$, $\tilde{\rho}_b\tilde{H}$, and $\tilde{\rho}_b\tilde{c}_w^2/\tilde{H}$, respectively . This

equation can be recast into a first-order system[1]:

$$\frac{\mathrm{d}v}{\mathrm{d}t} = Q \tag{18}$$

$$\frac{\mathrm{d}Q}{\mathrm{d}t} = \frac{1}{M}\left[-\frac{\mathrm{d}p}{\mathrm{d}t} - RQ - Kv\right] \tag{19}$$

This system was first solved by Tam and Auriault for use with the linearized Euler equations [6], and the resolution involved a ghost point for pressure. A direct implementation has apparently been used by Olivetti et al [21] for solving the Navier-Stokes in a turbulent channel flow. By direct implementation it is meant that Eq. (18) replaces the momentum equation in the direction perpendicular to the wall, at the grid point located on the wall. Olivetti et al mention a stability issue in some cases, but it is not clear whether it is a numerical or a physical one. We have also used successfully such a direct implementation before in a linearized Euler code (see Marx (2015) [14]), and in the linearized Navier-Stokes equations or the nonlinear disturbance equations. However, one of the boundary scheme was only second order to improve stability. Gabard and Brambley [13], and Brambley and Gabard [15] had a stability issue when using a direct implementation in the linearized Euler equations and used a characteristic formulation to stabilize their scheme. In this formulation, the ingoing acoustic wave is written as a function of the incoming one, which in spirit is similar to dealing with the reflection coefficient, as in Fung and Ju [36]. Here, since our solver is written in characteristic form, and motivated by the observation of Gabard and Brambley [13], the method of characteristics will be used to impose the MSD boundary condition for the Navier-Stokes equations. With this formulation we have not encountered stability issues.
In addition, at the wall one still has to enforce the non-slip boundary conditions u=0 and w=0, as well as the isothermal wall condition T=T_w. All together, these are four conditions that need to be imposed in the characteristic formulation. Moreover, four characteristic quantities need to be computed at the wall: Y^+, Y^-, Y^u, Y^s.

First note that due to the boundary condition u=0, one has: $X^+ = \frac{1}{\rho}\frac{\partial p}{\partial x}$ and $X^- = -\frac{1}{\rho}\frac{\partial p}{\partial x}$, leading to $X^+ + X^-$=0 at the wall. One has also X^s=X^v=X^w=0 at the wall. Due to the boundary condition w=0, one has similarly: $Z^+ + Z^-$=Z^s=Z^v=Z^w=0 at the wall. Accounting for these relations, and since one also has to satisfy $\partial u/\partial t$=0 at the wall, Y^u can fixed from Eq. (1). In the same fashion Y^w will be fixed in Eq. (3) to satisfy $\partial w/\partial t$=0. One has:

$$Y^u = -\frac{1}{2}(X^+ - X^-) + \frac{1}{\mathrm{Re}}\frac{1}{\rho}\frac{\partial \tau_{1j}}{\partial x_j}$$

[1]Refering to the discussion above, it is obvious that this set of equations is connected to the two ADE which would be used for computing the convolution integral for a second order system, although it is outside our scope to establish precisely this connection.

$$Y^w = -\frac{1}{2}(Z^+ - Z^-) + \frac{1}{\mathrm{Re}}\frac{1}{\rho}\frac{\partial \tau_{3j}}{\partial x_j}$$

To obtain the reflected wave Y^+ at the bottom wall from the incident wave Y^- one injects Eq. (18) into Eq. (2) to obtain:

$$Y^+ = Y^- + 2\left(\frac{1}{\mathrm{Re}}\frac{1}{\rho}\frac{\partial \tau_{2j}}{\partial x_j} - Q\right) \qquad \text{(bottom wall)} \tag{20}$$

For a rigid wall, the same relation holds with Q=0, this is Eq. (14). Equation (20) is the Navier-Stokes equivalent of the equation preceding Eq. (2.8) in Gabard and Brambley [13].

Finally, the isothermal character of the wall needs to be enforced, which imposes:

$$\frac{\partial s}{\partial t} = -\frac{(\gamma-1)}{\gamma}\frac{1}{p}\frac{\partial p}{\partial t} \qquad \text{(isothermal wall)} \tag{21}$$

Knowing $Y^\pm$ it is easy to compute $\partial p/\partial t$ and to deduce directly $\partial s/\partial t$ from this relation. Alternatively, in order to draw a parallel with the rigid wall case presented by Lechner et al. [28] we may further inject Eq. (5) and Eq. (4) in the latter equation to obtain:

$$Y^s = \frac{-1}{2c}(\gamma-1)(Y^+ + Y^-) + \frac{\gamma-1}{p}\frac{1}{\mathrm{Re}}\left[\Phi + \frac{1}{\mathrm{Pr}}\nabla\cdot(K\nabla T)\right] \tag{22}$$

$$\frac{\partial p}{\partial t} = -\frac{p}{2c}(Y^+ + Y^-) + pY^s \tag{23}$$

$$\frac{\partial s}{\partial t} = \frac{\gamma-1}{\gamma}\frac{1}{2c}\left(Y^+ + Y^-\right) - \frac{\gamma-1}{\gamma}Y^s \tag{24}$$

where $Y^s \neq 0$ arises from $v \neq 0$ for an impedance wall. For a rigid wall, one has Y^s=0 and these equations become equivalent to Eqs (15-16).

2.3.3. Numerical validation

The implementation of the MSD boundary condition is validated against the reference solution of Zheng and Zhuang [9] for the reflection of an initial Gaussian pressure pulse by a plane MSD wall. To remain in the linear inviscid regime in which the analytical solution has been derived, the amplitude of the pulse is small, and the thermo-viscous terms are all neglected (the solver is then a Euler equations solver).

The computational domain is a square box with $(x,y,z) \in$ [-50 50] $\times$ [0 100] $\times$ [-50 50]. The bottom MSD wall is at y=0, and on the other boundaries non-reflecting boundary conditions are used. The MSD characteristics, pulse size, and pulse-wall distance are the same as those used by Zheng and Zhuang [9]. Hence, we have: R=0.2; M=2.0938; K=0.4758, and the initial pressure (mean + pulse) is given by: $p(x,y,z,t{=}0) = \frac{1}{\gamma} + p_a e^{-\ln(2)/25(x^2+(y-30)^2+z^2)}$, where

the amplitude p_a=1e-8 is small. A regular mesh size is used in all directions, with Δx=Δy=Δz. Equal numbers of grid points are used in all directions, N_x=N_y=N_z. Figure 1 shows a comparison between the computed pressure and the analytical solution along the x-axis at t=30, obtained for Δt=0.5 and N_x=101. A very good agreement is observed. A convergence study has been

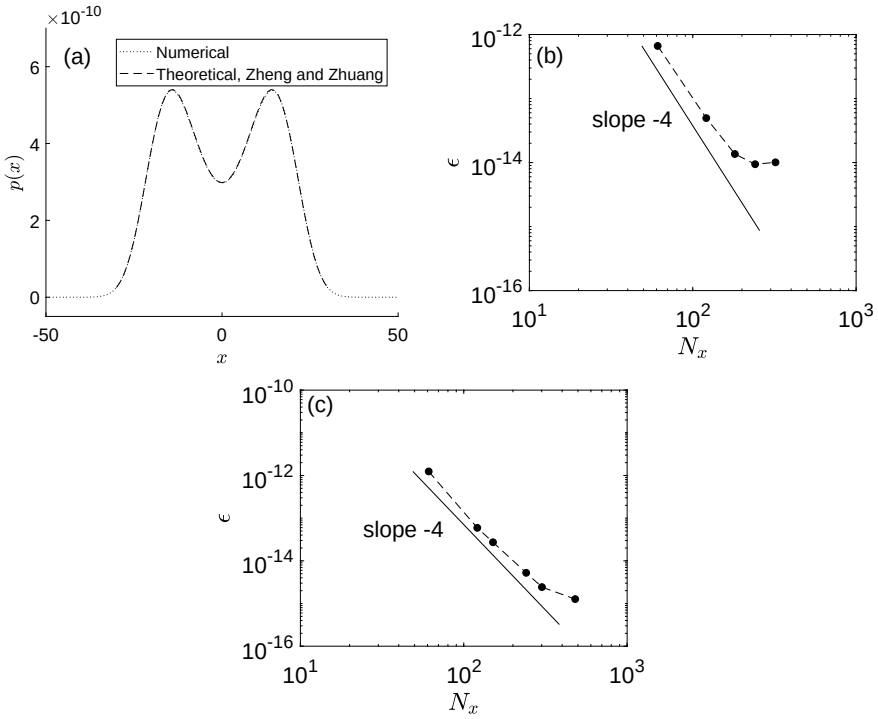

Figure 1: (a) Numerical vs theoretical pressure on the x-axis at time t=30 during Gaussian pulse reflection at an impedance wall. (b) Error (symbols) vs number of points in one direction for a fixed value of Δt=0.01. (c) Error (symbols) vs number of points in one direction for a fixed value of CFL=0.5.

performed by varying N_x (with N_y=N_z=N_x) for a small Δt=0.01 and is shown in Fig. 1(b). The order observed is about 4. It is not unusual to observe for the global order the order of the boundary scheme plus 1 [43]. As discussed earlier, one advantage of implementing directly Eq. (18-19) is that the order of the integration scheme should be preserved. This is now verified. The order of the Runge-Kutta method is 4. Since the spatial order has been found to be about 4, the truncation error is expected to be $O(\Delta t^4, \Delta x^4)$. Hence, by keeping CFL=$\Delta t/\Delta x$ constant, we should observe a global order $O(\Delta x^4)$. This is indeed verified to be the case in Fig. 1(c).

3. Mean flow statistics above the liner

In this section the statistics of a compressible turbulent flow in a channel having an impedance boundary condition at the bottom wall and a rigid upper wall are considered. The different test cases for which simulations (ILES) have been carried out are summarized in Table 1. Of particular interest is

Table 1: Impedance wall simulation test cases

Case	$\mathcal{M}$	R	ω_{res}	ξ	ω_{flow}	$\text{Re}_\tau^{\text{bot}}$	$\text{Re}_\tau^{\text{top}}$	$\Delta c_f^{\text{bot}}\%$	$\Delta c_f^{\text{top}}\%$
AC01	0.3	0.23	0.185	0.109	1.84	1031	476	575	44
AC02	0.3	0.23	0.367	0.109	1.84	642	434	162	20
AC03	0.3	0.23	0.738	0.109	1.84	523	411	74	7
AC04	0.3	0.23	1.479	0.109	1.84	453	399	31	1
AC05	0.3	0.23	2.960	0.109	1.84	397	392	0	-3
AC06	0.3	0.23	5.887	0.109	1.84	390	386	-3	-5
AC09	0.4	0.10	2.961	0.045	2.51	514	413	66	7
AC11	0.3	0.60	0.185	0.284	1.84	396	390	1	-2
AC12	0.3	1.00	0.185	0.474	1.84	393	391	-1	-2
AC13	0.3	0.3	0.185	0.142	1.84	854	461	367	36
AC14	0.3	0.4	0.185	0.190	1.84	626	434	151	21
AC15	0.3	0.5	0.185	0.237	1.84	440	399	24	1

the dependence of the flow on the resonance frequency of the liner and on its resistance. Several Mach numbers have been used, but all of them remain small. The resonance angular frequency of the material is defined as $\omega_{\text{res}} = \sqrt{K/M}$ (with a slight abuse of language, since strictly speaking this should be called the natural frequency). The liner may be characterized alternatively by the values of R, M, and K, or by the values of R, ω_{res}, and the damping ratio $\xi = R/(2\omega_{\text{res}}M)$. The latter quantities are provided in the table.

Recently, Scalo et al. [22] performed channel flow simulations with impedance walls, with Mach numbers up to $\mathcal{M}$=0.5 and resistance ranging from R=0.01-1. In addition, they tuned the resonance frequency of the liner so that it matches the typical angular frequency of the flow, defined to be: $\omega_{\text{flow}}=2\pi\mathcal{M}$. This frequency is typically high and much larger than the acoustic frequency that would be found in aeroengines. In the present work ω_{res} is first taken to be smaller than ω_{flow} for case AC01 and is progressively increased in the cases AC02-AC06, while keeping Re_b, $\mathcal{M}$, and R constant. The resistance is increased in cases AC11-AC12. Case AC09 corresponds to the smallest resistance used in this work and to a high resonance frequency.

The baseline frequency and resistance for case AC01 correspond to that for which an instability has been measured experimentally by Marx et al. [5], and the MSD characteristics are chosen to fit the impedance of the liner in the vicinity of the resonance frequency. The fit is the same as the one used

in Marx [45]. In dimensional units, this fit provides: $\tilde{R}$=94.4 kg m^{-2}s^{-1}; $\tilde{M}$=0.0685 kg m^{-2}; and $\tilde{K}$=2.71 10^6 kg m^{-2} s^{-2}. The resonance frequency is thus $\tilde{f}_{\rm res} = \tilde{\omega}_{\rm res}/(2\pi) \sim 1$ kHz, which corresponds to a realistic value for a liner. The normalized resistance $R \sim 0.23$ has a rather low value (lower than what would be found in practice in most aero-engines). In the experiments of Marx et al. [5], the half-height of the rectangular channel was $\tilde{H}$=0.01m and this value is used here to compute normalized numbers. In the experiment the friction Reynolds number upstream of the liner was $\mathrm{Re}_\tau \sim 3000$, which is costly to compute at the moment, even with a ILES. The simulations are thus performed at Re_b=6900, which corresponds to a smaller value of the friction Reynolds number, Re_τ=395. In the following we will compare the results of the present simulations with the direct numerical simulations of an incompressible channel flow with rigid walls at Re_τ=395 made by Moser et al. [46] (hereafter referred to as M395).

Case AC01 was performed in a computational domain of size $L_x \times L_y \times L_z = 6\pi H \times 2H \times \pi H$ (using a number of grid points $N_x \times N_y \times N_z = 351 \times 201 \times 125$). The domain size was chosen by running simulations on small domains to obtain the approximate wavelength of the structures in the direction of the flow. Then the domain length was increased to about two and then about three wavelengths to verify that the wavelength and flow statistics were stable. The independence of the statistics on the spanwise direction was then verified. The same procedure was followed for case AC02, leading to a domain size of $3\pi H \times 2H \times \pi H$, and this grid was then used for other cases for which the wavelength is smaller. For all the cases, we choose the grid resolution Δx^+=20 and Δz^+=10, with wall units based on the conventional channel at Re_τ=395. In the wall-normal direction, for case AC01, Δy^+ varies between 0.25 at the walls and 10 in the channel center, for case AC02 it varies between 0.5 and 10, whereas for the other cases Δy^+ varies between 1 and 10. A grid convergence study is provided in Appendix A.

3.1. Effect of the liner resistance R

The effect of liner resistance is first investigated. Olivetti et al. (2015) performed the simulation of a pipe flow with a liner having a resistance larger than 1 and reported that the turbulence statistics are not much modified by the liner, compared with a rigid wall [21]. Scalo et al. performed a series of simulations for resistance varying between 0.01 and 1 [22]. They observed important changes in the flow statistics for a low resistance value. The effect of resistance is presently investigated for 6 different values of the resistance: $R = 0.23$ (case AC01); $R = 0.3$ (case AC13); $R = 0.4$ (case AC14); $R = 0.5$ (case AC15); R=0.6 (case AC11); and R=1 (case AC12). The mean velocity profile and the rms of the axial velocity are plotted in Fig. 2. Also plotted is the M395 case for rigid walls. In this figure, and at several occasions in the following, with a slight but unambiguous abuse of notation, y represents the distance to the wall. For example, y is used rather than $y + 1$ for the bottom

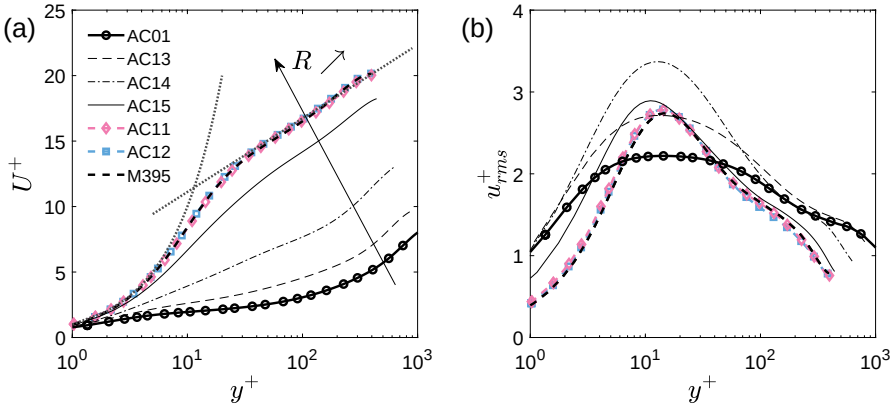

Figure 2: (a) Mean velocity profile and (b) rms of the streamwise velocity for varying resistance of the liner. Values of the resistance are $R = 0.23$ (AC01); $R = 0.3$ (AC13); $R = 0.4$ (AC14); $R = 0.5$ (AC15); R=0.6 (AC11); R=1 (AC12). In subplot (a), the straight dotted line indicates the log law, and the other dotted line the viscous sublayer (law of the wall).

lined wall located at y=-1. It is clear that for the lower resistance, $R \leq 0.5$, there are important changes in the flow statistics compared with the rigid wall, with at the lowest resistance a lower and broader peak of $u_{\rm rms}$ and a quasi-disappearance of the mean flow logarithmic region (it would be interesting to know if this remains true at higher values of the Reynolds number). The law of the wall is not followed either. For $R = 0.6$ and 1, the statistics are very close to the rigid wall channel statistics. This is in line with the findings in references [21, 22]. Hence, in the following we will focus on the configurations corresponding to a small resistance.

3.2. Effect of the resonance frequency $\omega_{\rm res}$

In this section we analyze the influence of the resonance frequency of the liner on wall turbulence in comparison with rigid wall turbulence. Cases AC01-AC06 are considered, which correspond to a constant value of Re_b and $\mathcal{M}$, and a given low resistance value R=0.23. The resonance frequency varies between $\omega_{\rm res}$=0.184 and $\omega_{\rm res}$=5.887. The typical frequency of the flow is $\omega_{\rm flow}=2\pi\mathcal{M}$=1.84.

The mean velocity profile for the different cases is shown in Fig. 3. For low resonance frequency (cases AC01-AC04), the mean profile departs from the reference profile M395 and the law-of-the-wall is not valid anymore. The flow speed is smaller in the vicinity of the bottom impedance wall and due to flow-rate conservation and the top wall being rigid, the flow speed is larger in the upper half of the channel. For the high resonance frequency cases, AC05 and AC06, the mean velocity profile follows the reference curve M395 for the rigid channel. Hence, for resonance frequencies somewhat higher than the flow

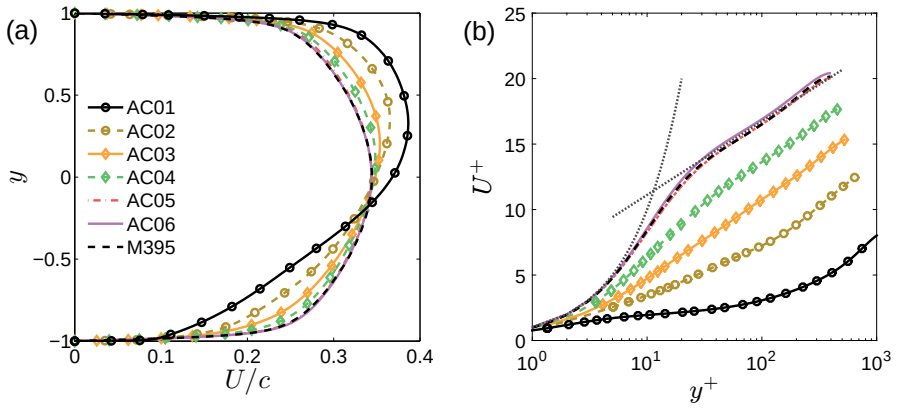

Figure 3: Mean velocity profile for varying resonance frequency of the liner as a function of the distance to the lined wall, scaled with (a) outer units c and H; (b) wall units u_τ and l_τ. In (b) the straight dotted line indicates the log law, and the other dotted line the viscous sublayer (law of the wall).

frequency, the MSD wall behaves as a rigid wall, even at low resistance.

Figure 4 presents the rms of stream-wise velocity, rms of wall normal velocity, Reynolds stress, and rms of streamwise vorticity. Unless specified otherwise, all quantities are non-dimensionalised using the wall-variables from the bottom impedance wall. For higher resonance frequencies (AC05-AC06) the turbulent statistics do not differ significantly from the ones for the rigid channel M395, which is the same behavior as for the mean velocity profiles. For the low frequency cases (AC01-AC04) noticeable differences are seen in the profiles of all quantities compared to the rigid wall channel M395. A broader peak in u_{rms} is seen in the buffer layer (as has been already noticed in Fig. 2(b) for AC01), and it occurs at a different location. This peak results from turbulence production, meaning the turbulence production is strongly affected by a low resonance frequency acoustic liner. Figure 4(c) shows that large values of the Reynolds stress are found close to wall for cases AC01-AC04, which indicates an increased momentum transfer in the turbulent flow throughout the channel. This transfer increases the drag as we will see below (see Section 5). In addition, a drop in ω_{xrms} is observed in Fig. 4(d) for these cases, and a similar drop of the other components of the vorticity (not shown here) is observed. It is well known that there exists a near-wall turbulence regeneration mechanism involving streaks and stream-wise vortices. This classical mechanism is highly disturbed for cases AC01 and AC02, the flow dynamics being strongly affected by the acoustic liner and the nonvanishing wall normal velocity at its surface. The value v^w_{rms} of v_{rms} at the wall does not vanish for a liner and decreases when ω_{res} increases, as seen in Fig. 4(b) (see also Table 2). We find that v^w_{rms} is roughly inversely proportional to the resonance frequency. For large resonance frequencies (cases AC05-AC06), $v^w_{rms} \to 0$, the liner behaves nearly as a rigid wall, and the statis-

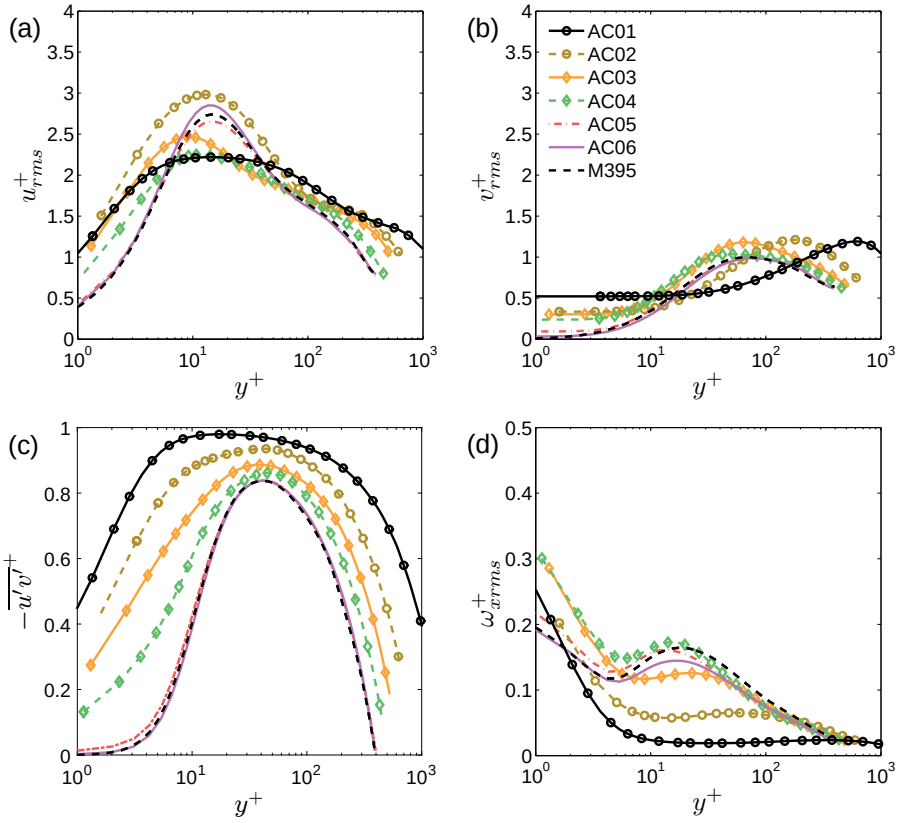

Figure 4: Profiles of (a) rms streamwise velocity; (b)rms wall-normal velocity; (c) Reynolds stress and (d) rms stream-wise vorticity for varying resonance frequency of impedance boundary condition.

tics of turbulence are close to those for a rigid wall, even for low value of the liner resistance.

4. Existence of a wave along the liner

In the previous section, it has been shown that for a liner with a resistance sufficiently small and a resonance frequency not too large, the statistics of turbulence differ from that of a turbulent channel flow with rigid walls. It is shown in this section that this is due to (or accompanied with) the presence of waves along the impedance surface. To evidence these waves the velocity spectra in the stream-wise direction are considered in Fig. 5. The axial wavenumber is denoted by k_x. The spectra are obtained at a position y=0.015 close to the impedance wall. The effect of the acoustic liner on the stream-wise spectra is clearly observed, as energy piles up at the resonance frequency, which leads to a partial modification of the turbulent energy cascade. For cases AC01-AC05

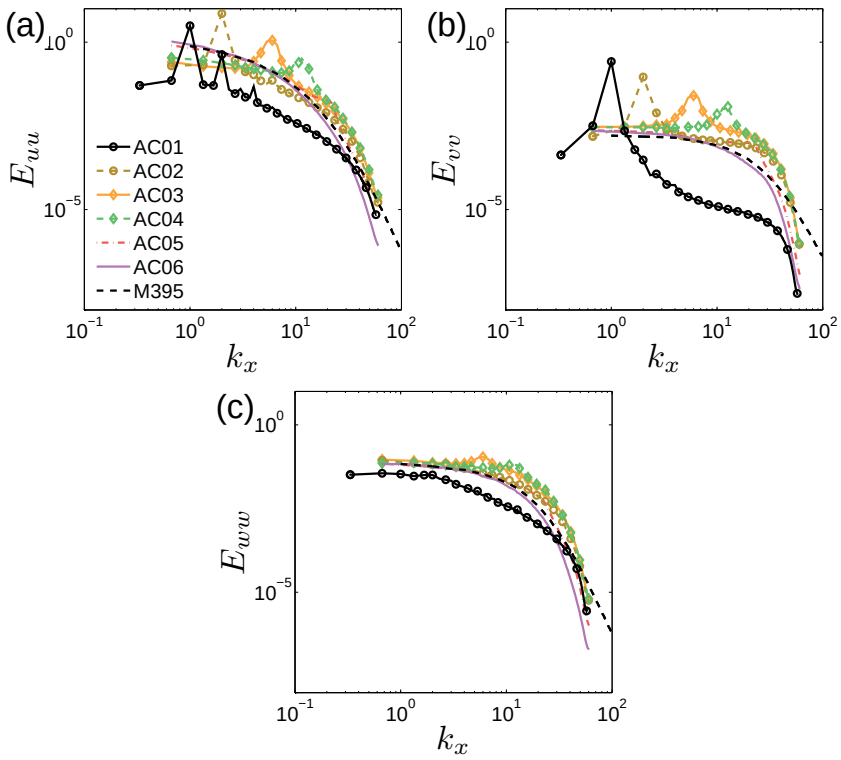

Figure 5: Velocity spectra of (a) streamwise velocity; (b) wall normal velocity; (c) spanwise velocity, versus the wavenumber k_x, at a location close to the wall (y=0.015), for several resonance frequencies (cases AC01-AC06).

we observe spikes in E_{uu} and E_{vv}, whose wave-number corresponds to the resonance frequency of the material (see Fig. 5a). We also find harmonics for case AC01. For cases AC03-AC04, we observe spikes in E_{ww}. Spectra for case AC06 are in good agreement with the spectra for a rigid wall (case M395). The angular frequency of the waves, ω_{wave}, has been computed from the peak of the Fourier transform of the wall-normal velocity measured at a point belonging to the liner surface. It is reported in Table 2. Overall, the observed frequency corresponds to the resonance frequency of the liner. For low values of ω_{res}, the convection speed for the surface wave, c_{wave}, is such that $c_{\text{wave}}/u_b \approx 0.6$. In order to assess if the vertical movement at the lined wall can perturb wall turbulence, the vertical displacement amplitude at the lined surface is estimated from $d_a = v^w_{rms}/\omega_{\text{wave}}$. In wall units it becomes $d_a^+ = d_a \text{Re}_\tau$, where the friction Reynolds number for a rigid wall is used here (Re_τ=395). For case AC01, d_a^+ is more than 50, which means that the vertical displacement from the wall goes well beyond the turbulence production region well known to be located at y^+=15. For case AC02, d_a^+ is also large. This explains why turbulence is so affected by the liner in these cases. As the resonance frequency increases the

Table 2: Characteristics of the wave along the liner: ω_{wave}, k_x, and c_{wave} are the measured angular frequency, axial wavenumber, and phase speed of the wave along the impedance wall, while v^w_{rms} is the rms of the wall-normal velocity computed at the impedance wall. The quantity d_a^+ is the estimated vertical amplitude of the displacement of a point on the lined surface, in wall units.

	AC01	AC02	AC03	AC04	AC05	AC06
ω_{res}	0.185	0.370	0.739	1.48	2.96	5.92
ω_{wave}	0.185	0.380	0.78	1.5	3.0	5.1
k_x	1	2	3	12.3	20.3	20.3
c_{wave}/u_b	0.61	0.62	0.42	0.41	0.49	0.87
v^w_{rms}	0.024	0.0094	0.0068	0.0047	0.0016	0.0005
d_a^+	51	10	3.5	1.2	0.21	0.039

value of the vertical displacement decreases. For cases AC05 and AC06, the displacement is less than d_a^+=1, and $y^+ = 1$ is often taken to be the first grid point position off the wall in large eddy simulations. Hence, for these two cases the wall displacement is too small to modify turbulence and turbulent statistics are similar to the rigid wall channel (M395), as observed above.

Some flow visualizations are now presented to illustrate the presence of the wave and show its effect on the flow. Instantaneous visualizations of the turbulent structures for the bottom half of the channel is shown in Fig. 6, where flow direction is from left to right. Among the displayed quantities is a slice of the wall-normal velocity component close to the wall (red color for blowing with v out of wall, and blue color for suction with v into wall). Also shown are iso-contours of Q2 events (ejections) and Q4 events (sweeps), colored with wall-normal location (darker shade close to wall and lighter away from the wall, blue (red) shade is used for Q2 (Q4) events). Iso-contours of the Q-criterion are finally colored in yellow to show the near-wall turbulent structures.

For the low resonance frequency case AC01, a large scale two-dimensional (2D) wave is clearly visible which propagates in the streamwise direction, with alternating blowing and suction regions. This wave strongly modifies and modulates the flow: structures (in yellow) are mainly present in the blowing regions and are absent in suction regions, leading to an inhomogeneous distribution of turbulent structures. In addition we do not see the near-wall streaks which are characteristic of the rigid wall turbulence, being an essential ingredient of its regeneration cycle. Q2 ejections are logically found in the blowing region (v out of wall), since the fluid is pushed away from the wall there, and Q4 sweeps are found in the suction regions (v into wall).

For the higher resonance frequency case AC04, waves of v at the impedance wall are observed, which are not 2D anymore and undulations are present in the spanwise direction. The Q2 and Q4 events are rooted in the impedance wall but tend to merge farther away from the wall where their scale become larger than the wavelength. This indicates an interaction between the flow

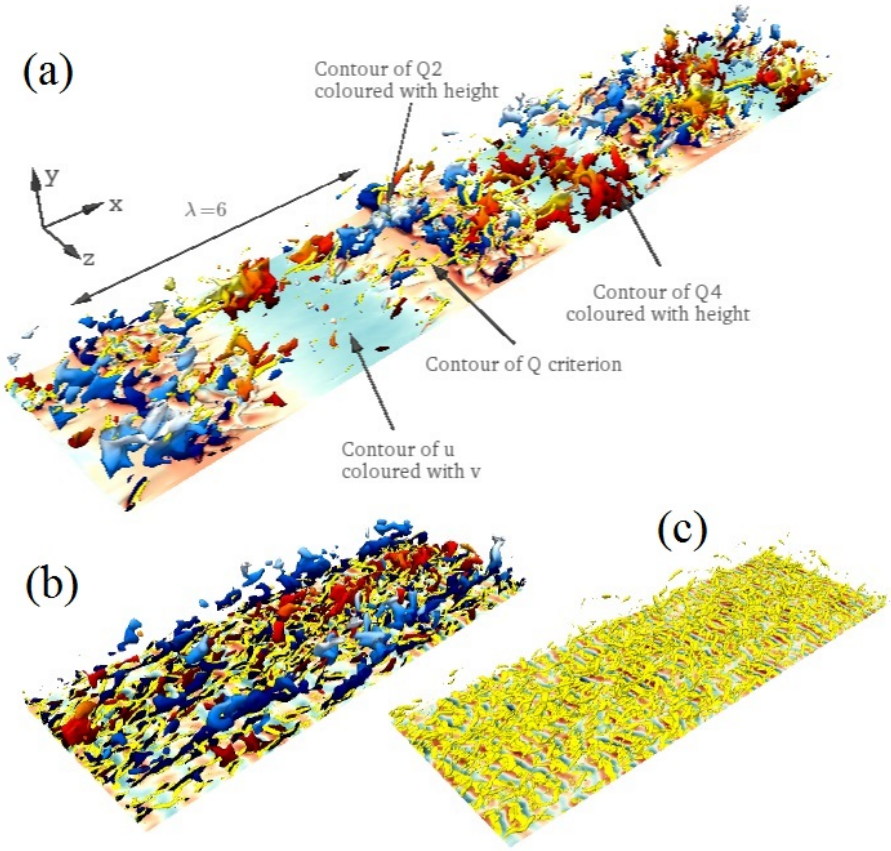

Figure 6: Instantaneous visualization of turbulent structures for the cases: (a) AC01, (b) AC04 and (c) AC09. Several quantities are shown: a colormap of v at the wall (light blue is for negative v corresponding to flow into the wall, light red is for v positive corresponding to flow out of the wall); iso-contours of $Q2^+$=-4, shown in blue and corresponding to ejection events; isocontours $Q4^+$=-4 shown in red and corresponding to sweep events; isocontours of Q-criterion Q^+=3 in yellow color.

and wave when $\omega_{\text{flow}} \approx \omega_{\text{res}}$. Unlike the flow for case AC01, the flow for case AC04 is densely populated with near wall turbulent structures. For cases with higher $\omega_{\text{res}} > \omega_{\text{flow}}$ (not shown here) we observe near-wall turbulent structures similar to rigid wall turbulence. This may not be the case if the resistance is smaller than for our baseline configuration AC01-AC06. For example, Fig. 6(c) corresponds to case AC09, where ω_{res} is large (but not much larger than ω_{flow}) and where the resistance is very small (R=0.1). In that case there is a large interaction between the small scales in the flow and the liner, leading to small spanwise rollers. Parameters for case AC09 are close to those used by Scalo et al. [22], and these authors observed very similar patterns along their impedance surface.

A slice of the instantaneous fluctuations of stream-wise velocity at wall distance y=0.03, and slices of wall-normal velocity and pressure at the wall are shown in Fig. 7. The computational domain being larger for case AC01, only a half of it is shown in the streamwise direction. For the low resonance frequency

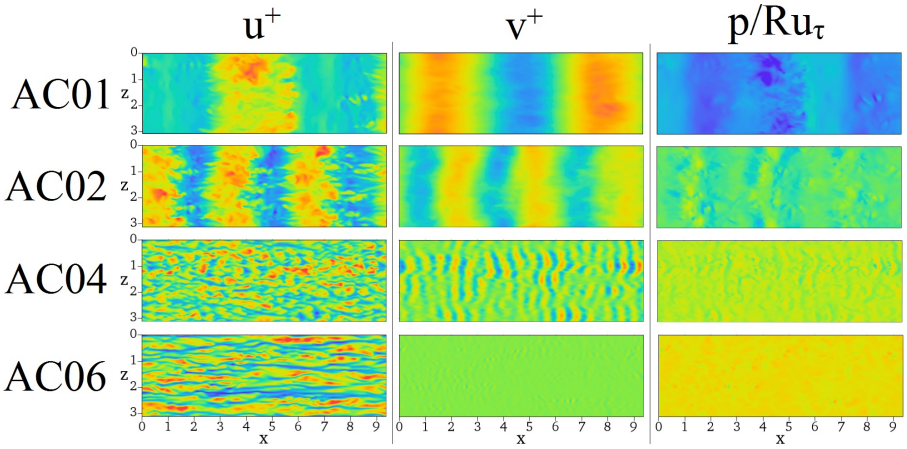

Figure 7: Slices of instantaneous fluctuations of u^+ (left) at wall distance y=0.03, and of v^+ (center) and p/Ru_τ (right) at the impedance wall for the cases AC01, AC02, AC04, and AC06. Blue (red) color corresponds to negative (positive) values, and the considered range is $-6 \leq u^+ \leq 6$, $-1 \leq v^+ \leq 1$ and $-6 \leq p/Ru_\tau \leq 6$ for all cases.

cases AC01 and AC02, waves are seen for all three variables. The waves are 2D with a phase difference of π between stream-wise and wall-normal velocity. As ω_{res} increases the wave progressively becomes less 2D. This is clearly seen in case AC04 (v component). For the high resonance frequency case AC06, elongated streaks are found close to the wall (left plot for u^+), which is the feature of rigid wall flows. No pressure wave is observed.

Hence, for a low resonance frequency, a wave is present along the liner surface. This wave has a rather two dimensional character which is lost as the resonance frequency increases and the wave length approaches the typical size of the structures in the flow. Phase averaging is now performed in order to obtain the spatial distribution of the wave. Phase averaging allows distinguishing between the effect of the wave and that of random turbulence. Phase averaging relies on the following triple decomposition [47] for any quantity a:

$$a = \overline{a} + a' = \overline{a} + \tilde{a} + a'' \tag{25}$$

where $\overline{a}$ is the Reynolds average, $\tilde{a}$ is the contribution from the wave, and a'' is the contribution from turbulence (note that depending on the context a tilde $\tilde{}$ is used either for a dimensional quantity or for a wave component). The extraction of the wave is based on phase averaging: $\tilde{a}(\phi) =< a >_\phi$ where $< \cdot >_\phi$ is the

phase average, that is, the average over all the available samples corresponding to the same phase ϕ, with $0 \leq \phi < 2\pi$. When the wave results from some periodic external triggering, the phase reference for phase-averaging is provided by this external trigger. Here the wave is self excited and we cannot rely on such external reference. However, in cases where the wave is two-dimensional its normal component v at the impedance wall is not noisy (see Figs. 6 and 7) and sinusoidal; the phase of v at the wall is thus taken as the phase reference. The procedure used to extract the wave (amplitude and phase angle) is thus the following:

1) For any flow field, average v at the wall in the span-wise direction to obtain a periodic 1D wave of v in the flow direction. This is legitimate as long as the wave is 2D; 2) Define several phases within a period (in the present case we use 12 bins); 3) For any component (u,v,...) assign a phase bin to any streamwise position. This phase bin is simply taken to be that of the 1D wave of v which serves as a phase reference; 4) Compute the phase averaged components at each phase, by averaging the samples corresponding to the same phase bin; 5) Subtract the global mean to obtain wave profiles at each phase; 6) Compute the amplitude and phase angle of the waves using the wave profiles at each phase. Several instantaneous flow fields are used for this process. The random components a'' can then be obtained by subtracting the global mean $\overline{a}$ and the phase average $\tilde{a}$ from instantaneous fields. 2D surface waves which go all the way up to the channel center are obtained at low values of ω_{res}. Hence, we limit ourselves to cases AC01-AC03 for the phase averaging. Satisfactory 2D surface waves are observed for cases AC01 and AC02. However we do not expect entirely trustworthy results from AC03 where the 2D character is partially lost.

The amplitude of the phase-averaged stream-wise and wall-normal velocity, denoted respectively by $|\hat{u}(y)|$ and $|\hat{v}(y)|$, are shown in Fig. 8. The stream-wise

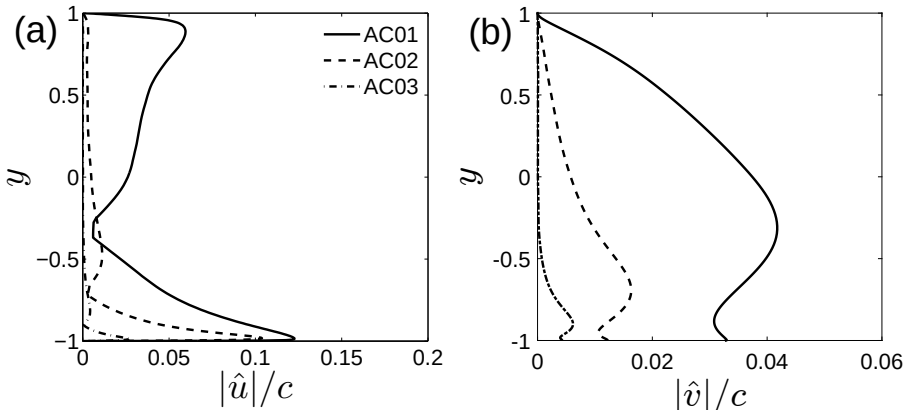

Figure 8: Amplitude of the wave along the liner: (a) stream-wise velocity component; (b) wall-normal velocity component.

velocity component of the wave is larger close to the wall, and the maximum

decreases as the resonance frequency increases. For the wall-normal velocity component, the peak amplitude is obtained away from the wall, and also decreases when $\omega_{\rm res}$ increases. Some characteristics of the wave (wavelength, phase speed) were given in Table 2. The shapes in Fig. 8 are reminiscent of the wave measured and modeled by Marx and Aurégan [25] (see their Fig. 14 where normalized eigenfunctions for u and v are given). However, in the present case the wave is not in its linear regime. More details are given in Section 6. The eigenfunctions given here also resemble those obtained by Jimenez et al [23] for a pure resistance (actually these authors replace their resistive wall by a controlled wall actuation to perform a phase average process similar to the one performed here).

5. Drag increase

In this section it is shown that the modifications in the flow induced by the liner are associated with an increase in the drag, compared with the channel with rigid walls. The friction at the wall is classically measured by Re_τ defined in Eq. (13). This is given in Table 1 for both the bottom impedance wall and the top rigid wall. Other useful quantities are the drag coefficient and the change in drag coefficient in percent computed as follows:

$$c_f = \frac{2\tau_w}{\rho_w u_b^2} \tag{26}$$

$$\Delta c_f\% = \frac{c_f - c_f^{\rm ref}}{c_f^{\rm ref}} \times 100 \tag{27}$$

The change in drag is computed with respect to the conventional channel flow M395, $c_f^{\rm ref}$ being the drag coefficient for case M395. Thus, a positive value indicates a drag larger than the drag in a channel flow with rigid walls. $\Delta c_f\%$ is indicated in Table 1 for both walls. Table 1 shows that the friction at the impedance wall is more important than for the rigid channel in the cases for which the flow modifications are important. This is the case for low resistance and a not too large resonance frequency, that is for cases AC01-AC03, AC13-AC15, and case AC09. For three of these cases a flow visualization has been shown in Fig. 6. For case AC01 the drag is increased by as much as 575%.

The connection between the wave along the liner and the drag increase is now discussed. Using the phase-averaging process introduced in the previous section, it is possible to compute the drag increase at each phase of the wave. This is shown in Fig. 9(c).

The phase averaged wall-normal velocity at the impedance wall, which is used as reference for phase averaging, is also presented in the figure. Phases Φ=0 (and 2π) correspond to blowing (v out of wall) and phase Φ=π to suction (v into wall). We see that during suction we have an important increase in drag, with $\Delta c_f\%$ multiplied by a factor 22 for case AC01 for $\Phi = \pi$, due to a strong impingement of the flow at the wall. Averaged over a period the drag

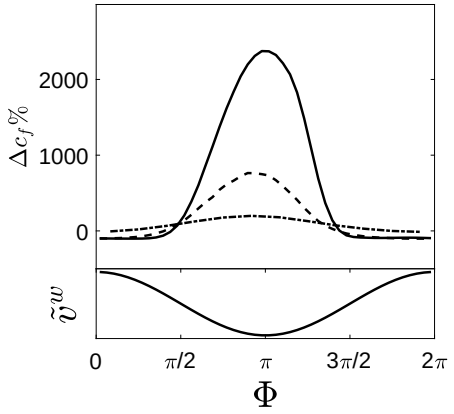

Figure 9: Phase-averaged drag increase in percent (for reference, the vertical component of the wave at the wall is also indicated in the bottom of the plot).

increase is 575% (Table 1). Remember from Fig. 6 that for case AC01 no turbulent structures are present in suction regions. Hence, the drag increase is not due to the effect of turbulence, but rather to the effect of the wave, which brings in high speed flow to the wall. Figure 9c also shows that there is a small drag reduction ($\Delta c_f\% < 0$) during blowing for cases AC01 and AC02.

We now consider the total Reynolds stress $\overline{u'v'}$. Using the triple decomposition, this can be decomposed into several contributions:

$$\begin{aligned} \overline{u'v'} &= \overline{(\tilde{u}+u'')(\tilde{v}+v'')} \\ &= \overline{\tilde{u}}\overline{\tilde{v}} + \overline{u''v''} + \overline{\tilde{u}v'' + u''\tilde{v}} \end{aligned} \tag{28}$$

The 3 contributions are those from the wave, from the turbulence, and from cross terms. In the original triple decomposition [47] these cross terms are null because the wave and the turbulence are supposed to be uncorrelated, but such an assumption cannot be made a priori in the present case when the wave can modulate the turbulence. Nevertheless, it has been verified that the contribution of these terms is very small. The contributions for the other two terms are shown for case AC01 in Fig. 10. Wall units based on the bottom impedance wall are used for the scaling, therefore the peak values close to the top rigid wall have a small magnitude. Close to the impedance wall, the major contribution to the Reynolds stress comes from $\overline{\tilde{u}}\overline{\tilde{v}}$, whereas away from the wall it comes from $\overline{u''v''}$. Hence, close to the wall an increased momentum transfer is due to the wave, and since $\overline{\tilde{u}}\overline{\tilde{v}}$ is negative, momentum is transferred to the wall, which contributes to increasing the drag. This is in agreement with the drag increase being correlated with the wave, as observed above in Fig. 9(c).

It is interesting to draw a parallel between the wave created here spontaneously in the vicinity of the liner and the waves that are sometimes imposed

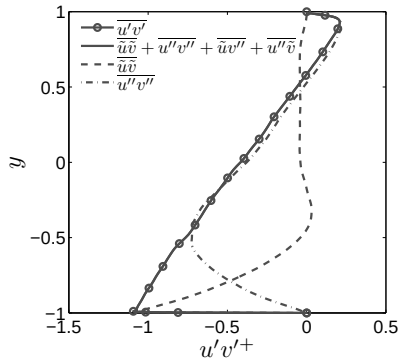

Figure 10: Contributions to the Reynolds stress $\overline{u'v'}$, scaled with u_τ and ρ_w from the bottom impedance wall. Case AC01.

using blowing and suction (or some related forcing) in flow control [48, 49, 50]. In flow control it is well known that the surface waves resulting from blowing/suction should generally have a negative phase speed to obtain a drag reduction. For example Mamori and Fukagata [49] performed simulations of a channel flow with a wave-like wall-normal body-force. For upstream traveling waves (having a propagation speed smaller than the bulk velocity) they find a drag reduction of up to 40%. They reported the presence of span-wise rollers which produces positive $\overline{u'v'}$ close to wall and contribute to reducing the drag. Here in Fig. 10 we find the opposite behavior since the wave has a positive phase speed and $\overline{\tilde{u}\tilde{v}}$ is negative, leading to a drag increase. In our case the wave is formed spontaneously by the interaction between the flow and the boundary condition, thus it is not a controlled configuration. Hœpffner and Fukagata [50] study wall actuation, such as wall deformation or wall blowing and suction. They argue that both actuation can be characterized as pumping and this pumping is strongly connected to drag reduction. Here the drag increases as a result of the phase between the $\tilde{u}$ and $\tilde{v}$ components of the wave, and this also corresponds to some pumping by the wave. The acoustic liners produce a wave with a phase speed in the flow direction and a magnitude of the order of u_b and it is unlikely that they can be used for passive drag reduction. Nevertheless, a slight drag decrease is reported for some cases in Table 1.

6. Stability analysis

In this section it is shown that the wave observed above the liner can be connected to an unstable surface wave. In the literature there has been several investigations of the surface wave modes in flow duct acoustics [51, 52, 53, 54, 45, 25]. All these investigations have been done in a spatial frame of work, in which the (real) mode frequency is given and the (complex) mode wavenumber

is computed. This is the traditional way of computing a wavenumber spectrum in acoustics. In the present case, since the computational domain is periodic in the flow direction, a temporal analysis is more relevant: the (real) wavenumber k_x is given, and the spectrum of the (complex) angular frequency $\omega = \omega_r + \mathrm{i}\omega_i$ is computed. Temporal analyses have been performed by Jimenez et al [23] for a purely resistive surface, by Tilton and Cortelezzi [55] for a model of porous surface, and by Rahbari and Scalo [57], again for a purely resistive surface. Also, it should be mentioned that global stability analyses have been performed recently by Pascal et al [56] and Rahbari and Scalo [58].

Both the linearized Euler or Navier-Stokes equations, possibly complemented with a turbulent eddy viscosity model, are encountered for modal analysis. Normally, an unstable surface mode is found by using an inviscid model, and including the dissipative phenomena provides a better estimation of its characteristics [25]. In the present work, the two-dimensional linearized Navier-Stokes equations for compressible perturbations are employed. Given the low Mach number used in the numerical simulations, the shear base flow $U_0(y)$ for the linearization is almost incompressible, and the mean density and temperature are uniform. The equations are given in Eqs. (B.1-B.5) presented in Appendix B, where the same normalization (see Section 2.1) as for the numerical simulation is used. These equations are discretized in the wall normal direction in the same way as in Ref. [25], which leads to the eigenvalue matrix problem in Eq. (B.6). The MSD boundary condition at the bottom wall at y=-1 is easily included in this eigenvalue problem, see Eq. (B.16-B.17). The top wall at y=1 is rigid. The solution of Eq. (B.6) relies on standard librairies [25], and provides for each value of the wavenumber k_x an eigenvalue spectrum ω. The solver has been validated against spatial solvers that have themselves been extensively validated [25].
In the following, the spectrum of standard canonical flows are first considered briefly to show how a MSD wall can lead to instability before the method is applied to the numerical simulation.

6.1. Instability due to MSD

A parabolic mean flow $U_0(y) = U_c(1 - y^2)$ for a channel with rigid walls is first considered, where U_c=0.1 is the velocity at the center of the channel (which is related to the Mach number $\mathcal{M} = 2U_c/3$ given the normalization with the speed of sound). For a Reynolds number based on the center velocity of Re_c=2000 (Re_b=2/3Re_c) and k_x=1 this flow is known to be stable in the incompressible regime [59], which is confirmed by the spectrum of the phase speed $C = \omega/k_x = C_r + \mathrm{i}C_i$ presented in Fig. 11(a). Indeed, all eigenvalue have $C_i < 0$ (that is, also $\omega_i < 0$), meaning the flow is stable. Acoustic modes are indicated by square symbols. The inviscid limit for these modes in a uniform flow of Mach number $\mathcal{M}$ is given by:

$$\omega = k_x\mathcal{M} \pm \sqrt{k_x^2 + \left(\frac{n\pi}{2}\right)^2} \qquad \forall n = 0, 1, 2, \cdots \tag{29}$$

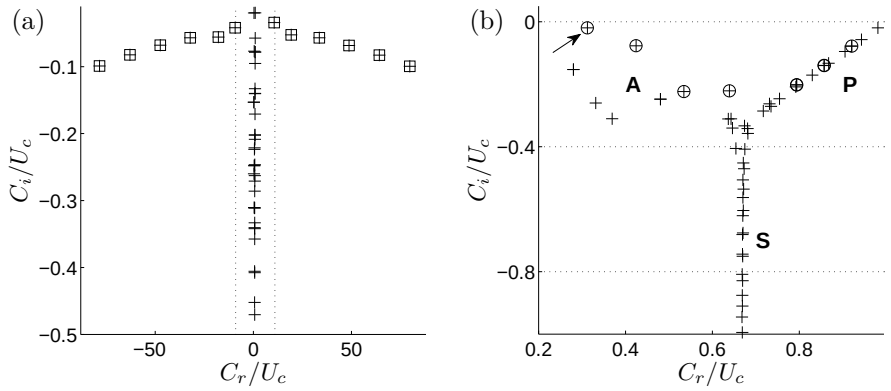

Figure 11: Complex phase speed spectrum (+) for a parabolic flow with rigid walls and k_x=1, Re_c=2000. (a) Full spectrum. Symbols (□) indicate the acoustic modes; The vertical dotted lines are at $C_r/U_c = 1+1/U_c$ and $C_r/U_c = 1-1/U_c$. (b) Zoom in on the non-acoustic modes. Symbols (○) are some reference values obtained for an incompressible flow.

Two vertical lines indicate the speed $U_c - c_w = U_c - 1$ and $U_c + c_w = U_c + 1$, which are the propagation speeds of the upstream and downstream plane sound waves. The modes located outside the region comprised within the two vertical lines are all non-plane acoustic modes. Figure 11(b) presents a zoom in of the region within the two vertical lines. This region consists of non-acoutic modes. It classically displays a Y-shaped spectrum with 3 branches denoted A, P, and S. The A-branch modes are often designated as wall modes because their eigenfunctions are maximal close to the walls. The P modes are designated as center modes, since their eigenfunctions reach their maxima close to the channel center. Some reference values for an incompressible flow (given in the appendix A.7 of reference [59]) are added to the plot: for the low Mach number value U_c=0.1 taken here the agreement between the present results and the reference value is already quite good (the agreement can be reached at any order of accuracy by lowering compressibility by reducing the value of U_c).

The effect of the MSD boundary condition on stability is now evidenced. The particular mode shown by an arrow in Fig. 11(b) belongs to the A-branch for rigid walls and corresponds to C/U_c ∼0.31-0.020i and ω ∼0.031-0.0020i. The bottom wall of the channel is now changed from rigid to MSD, and the MSD resonance frequency is taken to match the frequency of that particular mode, with $\omega_{\mathrm{res}} = \sqrt{K/M}$ ∼0.031. The resistance is given an arbitrary small value, R=0.0001, all other parameters being unchanged. The corresponding spectrum is shown in Fig. 12(a). A new mode, indicated by an arrow, stands just above the original particular mode chosen. This new mode has a small positive value $C_i \sim 0.00002$, indicating that the flow is now unstable, other modes remaining approximately the same. By modifying the resonance

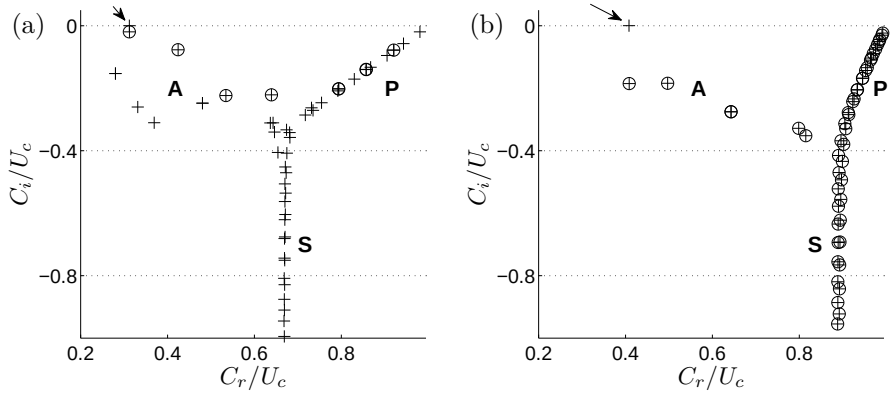

Figure 12: (a) Complex phase speed spectrum (+) for a parabolic flow with a top rigid wall and a MSD bottom wall tuned to resonance frequency 0.031. k_x=1, Re_c=2000. The reference values for the incompressible flows with rigid wall are still indicated (∘). (b) Comparison of the spectra obtained for a $U_c(1-y^8)$ profile with a top rigid wall and: (∘) a bottom rigid wall; (+) a bottom MSD wall tuned at the correct resonance frequency. k_x=1, Re_c=2000.

frequency of the MSD wall, we have observed that it is possible to render unstable any mode of the A-branch and many modes of the P-branch. However, the modes with the highest growth rate are those with a lower value of C_r. Hence, a MSD wall can prompt some modes to become unstable, particularly those of the A-branch. Unstable modes above liners are often called surface waves due their fast decrease away from the wall. This is in agreement with these modes arising from the A-branch of wall modes. Tilton and Cortelezzi [55] for a porous surface, and Rahbari and Scalo [57] for a purely resistive surface, observed that two modes may be unstable due to the channel walls not being rigid, one symmetric, and one anti-symmetric. The mode obtained here for a resonant material is very similar in nature to their symmetric mode (as a result of only the bottom wall being non-rigid in the present study). Hence, qualitatively, purely resistive, porous, and resonant surfaces all give birth to the same type of instability.

A mean flow with a steeper profile $U_0(y) = U_c(1-y^8)$ (let us call it "turbulent like") is now considered, again with k_x=1, Re_c=2000. The spectrum for rigid walls is shown with ∘ symbols in Fig. 12(b). Overall, compared with the parabolic profile, the spectrum is shifted toward higher phase velocities. All eigenvalues are found in the bottom half plane, indicating that the flow is stable. The spectrum obtained by replacing the bottom rigid wall by a MSD wall is shown with + symbols in Fig. 12(b). The resonance frequency is tuned to the frequency of the leftmost mode of the rigid wall case (corresponding to $\omega_r \sim 0.04$, or $C_r/U_c \sim 0.4$). With a MSD bottom wall, a slightly unstable mode (indicated with an arrow) is appearing on top of the leftmost stable mode. All

other modes are unchanged. This is the same behaviour as for the parabolic profile. Only the modes pertaining to the A-branch could be destabilized in that way. The normalized norm of the streamwise velocity eigenfunction is given in Fig. 13 for both the parabolic and eigth-power velocity profiles. For

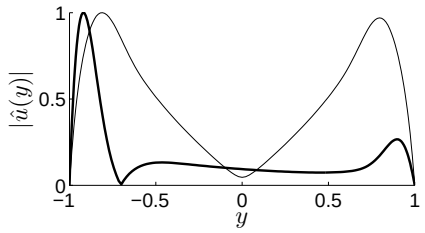

Figure 13: Streamwise velocity eigenfunction (normalized to have unit maximum) for the unstable mode for: —— the parabolic mean velocity profile with $U_0(y) = U_c(1 - y^2)$; ▬ the steeper profile $U_0(y) = U_c(1 - y^8)$. k_x=1, Re_c=2000. The bottom wall at y=-1 is of the MSD type.

the parabolic flow, the maxima close to the rigid and MSD walls are about the same. For the steeper profile, the peakedness of the eigenfunction close to the MSD wall is more pronounced and resembles the shape of a surface mode.

In this subsection, the major ingredients for the temporal stability of a channel flow with a bottom MSD wall have been given. If the MSD wall is tuned to the frequency of the modes of the A-branch, these modes can be destabilized. The destabilization is more effective for the modes located on the left of the A-branch. This is also where the classical Tollmien-Schlichting (TS) unstable wave can be found at higher Reynolds numbers. There is thus some similarity between this TS wave and the present liner-due surface mode, although the latter can exist even without viscosity. Note that Jimenez et al [23] argue that for a fully permeable surface (purely resistive with zero resistance), the mode is connected to a Kelvin-Helmholtz instability.

6.2. Comparison with the numerical simulations

The waves observed in the numerical simulations and reported in Section 4 for cases AC01-AC03 are 2D waves, and we now try to explain their presence by the same type of 2D stability analysis as in the previous subsection. These waves are non-linearly saturated waves not really prone to a linear stability analysis. To circumvent this limitation the following method that has been employed: the configurations AC01, AC02, and AC03 were run with a bottom *rigid* wall rather than a MSD wall until a statistically stationary turbulent channel flow is observed. Then at some instant chosen as the origin of time, $t = 0$, the bottom rigid wall is suddenly replaced by a MSD wall. Due to the flow being unstable, an instability develops in the numerical simulation in the vicinity of the bottom

wall and for some time it should be linear.

The base flow $U_0(y)$ for the stability analysis should be close to be the actual mean velocity profile of the turbulent channel flow with rigid walls at Re_b=6900 (Re_τ=395), which is the profile when the MSD wall is set up at t=0. The numerically calculated profile could be used but it is more convenient to use an analytical velocity profile that matches this mean flow. In particular this avoids the need for interpolation, and facilitates grid convergence study. As in reference [25] (see Eqs (3-4) therein), the Cess mean velocity profile is used for that purpose. It is indeed verified in Fig. 14 that it is a very good approximation to the computed mean flow. However, since the unstable mode is known to be sensitive to the velocity profile, results obtained with the actual mean velocity profile (interpolated on the Chebyshev grid) will also be presented in some places (Table 3, Fig. 17(b)).

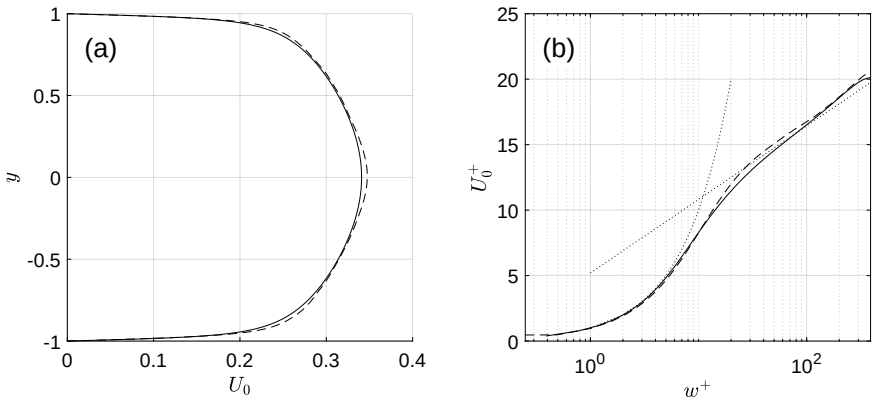

Figure 14: Comparison of the mean velocity profile obtained numerically (dashed line) with *rigid* walls and the analytical Cess profile (plain line). (a) in outer units; (b) in wall units ($w = y + 1$ represents the distance to the bottom wall).

The time evolution of the amplitude of the dominant spectral component (spectral refers to Fourier transform in the x-direction) of the wall-normal velocity v on the bottom MSD wall is shown in Fig. 15(a), for case AC02. The value of the streamwise wavenumber k_x corresponding to this maximal spectral amplitude is given in Fig. 15(b). Before saturation starts at time t ∼150 the amplitude corresponds to a constant value of k_x=3.55 and exhibits an exponential growth typical of an instability. At later times, saturation leads to a final state that is the same as described in Section 4, and the wavenumber corresponding to the final state (k_x ∼2 in Fig. 15(b), see also Table 2) differs from the wavenumber for the initial instability (k_x=3.55). The characteristics of this instability (wavenumber, angular frequency, growth rate) are computed for t <150 and compared to those predicted by the stability analysis. The characteristics of the wave extracted from the numerical simulations is compared

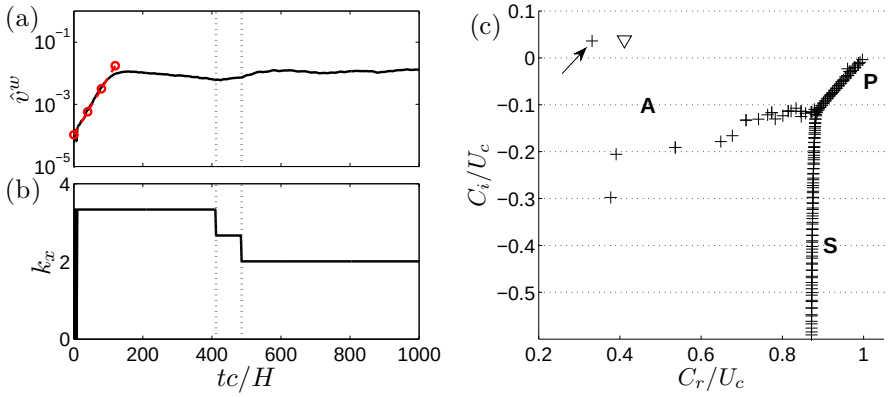

Figure 15: For case AC02: (a) Time evolution of the spectral component of the wall-normal velocity at the impedance wall having the largest amplitude (the straight dashed line with symbols is a fit to the initial exponential growth); (b) Streamwise wavenumber of the spectral component having the largest amplitude; (c) Normalized phase speed spectrum (+) resulting from a linear stability analysis performed for k_x=3.55. The triangle is the phase speed computed from the numerical simulation.

to that of the stability analysis in Table 3. For the numerical simulation the characteristics are the one of the observed wave. For the stability analysis, a search of the most unstable mode has been done, and the reported value of k_x is the one for which the largest value of ω_i is obtained. The stability analysis has been performed for the Cess mean velocity profile and the numerical mean velocity profile. The latter is computed for rigid walls, just before the bottom MSD wall is introduced at $t = 0$. The characteristics predicted by both profiles are reasonably close, and if not perfect, the agreement with the numerical simulation is satisfactory. For example, for case AC02 the wavenumber k_x and the growth rate ω_i agree rather well. In any case the value of ω_r is slightly larger than the angular resonance frequency of the liner, $\omega_{\text{res}} = \sqrt{K/M}$. Figure 15(b) shows the spectrum predicted by the stability analysis, for case AC02. It bears many similarities with that for the canonical eigth-power velocity flow considered above. In particular, the unstable mode indicated by an arrow stands on the left side of the A-branch. The mode calculated from the numerical simulation is indicated with a triangle symbol. The eigenfunctions for the streamwise and wall normal velocities for case AC02 are compared in Figs 16(a) and 16(b), respectively. Both are normalized with the value of the wall normal velocity eigenfunction at the wall.

If the values are not exactly the same, especially for $\hat{u}$, the general trends are similar. The eigenfunctions for the saturated state obtained at large times (which were already included in Fig. 8) are also shown. Obviously the saturated state will differ in many respects of the initial instability leading to this state. Nevertheless, some similarities exist between the eigenfunction in the two

Table 3: Comparison between the characteristics of the instability wave observed in the numerical simulation during the growth period and the characteristics of the most amplified wave predicted by the linear stability analysis. For the stability analysis, either the Cess velocity profile or the numerical profile have been used.

Case	ω_{res}	Numerical			Stability Analysis					
		Simulation			Cess profile			Numerical profile		
	$=\sqrt{K/M}$	$k_x^{\max}$	ω_r	ω_i	k_x	ω_r	ω_i	k_x	ω_r	ω_i
AC01	0.185	2.3	0.22	0.028	1.65	0.210	0.0282	2.1	0.22	0.030
AC02	0.367	3.3	0.47	0.044	3.55	0.408	0.0445	4	0.41	0.051
AC03	0.738	6.7	0.79	0.073	7.05	0.787	0.0585	7.3	0.79	0.073

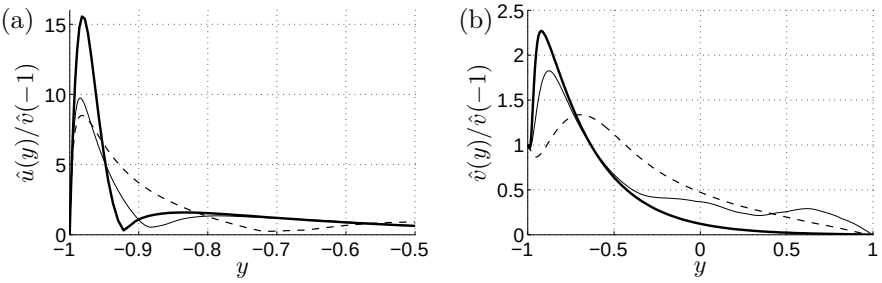

Figure 16: (a) Streamwise velocity eigenfunction. (b) Wall normal velocity eigenfunction. Case AC02. k_x=3.55. ——— Stability analysis; —— Numerical computation, during the exponential growth of the instability; - - - Numerical computation, final saturated state.

regimes, which tends to indicate that the dynamics of the wave observed in the vicinity of the lined wall in Section 4 is partially governed by a linear instability.

6.3. Link between resistance, growth rate, and observed drag increase

A critical value of the resistance is expected for a liner, above which there should be no instability. Moreover, the drag increase observed in the numerical simulations is due to the wave along the liner, and this wave is partly governed by a linear instability. Hence, it is also expected that the predicted growth rate of the instability and the observed drag increase should be correlated below the critical resistance. This is now investigated.

A linear stability analysis is performed for case AC01 in table 1. The baseline resistance for case AC01 is $R = 0.23$. However, the resistance is here allowed to vary from $R = 0.01$ to $R = 0.8$ so that its effect can be investigated. The growth rate as a function of the wavenumber is shown for the unstable mode

in Fig. 17(a), for several values of R. For each R the growth rate is maximal for some given wavenumber, as indicated with a filled symbol. The maximal growth rate is given as a function of resistance in Fig. 17(b). It is confirmed that there exists a critical resistance $R = 0.7$ above which configuration AC01 is stable (configuration AC02 is also shown, and corresponds to a critical resistance $R = 0.6$). It is verified for case AC01 in Fig. 17(b) that using the numerical velocity profile in the stability analysis rather than the Cess profile has almost no effect on the critical resistance. In addition, the growth rate increases linearly as R decreases and saturates as the resistance approaches a zero value. The angular frequency of the instability obtained at the wavenumber corresponding to maximal growth is given in Fig. 17(c) for both AC01 and AC02 cases. Also indicated in this figure is the theoretical resonance frequency for a damped oscillator[60], given by $\sqrt{K/M - (R/2M)^2}$ (a more precise definition compared to $\omega_{\text{res}} = \sqrt{K/M}$ used everywhere else in this paper). The frequency of the instability in the presence of flow is classically larger than this theoretical value, but follows the same trend. In particular, the frequency of the most amplified instability saturates to a value slightly larger than $\sqrt{K/M}$ when $R \to 0$. This would not be the case for a purely resistive system (such as considered by Jimenez et al [23] or Rahbari and Scalo [57]), in which the frequency of the most amplified instability (as well as the corresponding wavenumber) would increase importantly as $R \to 0$. Finally, the phase speed of the most amplified instability is given as a function of resistance in 17(d) for case AC01. The phase speed decreases with decreasing R. It would appear that this is opposite to the observations by Rahbari and Scalo [57] (see their Fig. 6) that the phase velocity increases when R decreases, at a fixed wavenumber. However, even for a purely resistive liner, we have verified that the phase velocity decreases when R decreases as long as the wavenumber is changed along with R to always correspond to maximal growth (if α is fixed instead, we also find that the phase speed increases with decreasing R). This means that the qualitative behavior of the phase speed is the same for a purely resistive and a MSD liner. For the original AC01 case (with $R = 0.23$), the phase speed in Fig. 17(d) is $c_{r,max}/u_b \sim 0.42$. This is less than the value $c_{wave}/u_b = 0.61$ reported in Table 2. However, this difference is logical, since the latter value corresponds to the saturated state, whereas $c_{r,max}/u_b \sim 0.42$ corresponds to the initial linear instability. Since the wavenumber decreases (as shown in Fig. 15(b) for AC02) as the instability saturates, and meanwhile the frequency does not change much, the phase speed increases during saturation.

The drag increase obtained in the numerical simulations (as reported in Table 1) for cases AC01, AC13, AC14, AC15, AC11, and AC12 (all corresponding to baseline configuration AC01 with different values of R) is plotted in Fig. 18. The drag increase here corresponds to the saturated state. Below a critical resistance, the value of which is between $R = 0.5$ and $R = 0.6$, the drag increase decreases approximately linearly with increasing resistance, which is in line with the predicted growth rate of the linear instability also decreasing linearly with resistance (see Fig. 17(b)). Moreover, the critical resistance observed in the

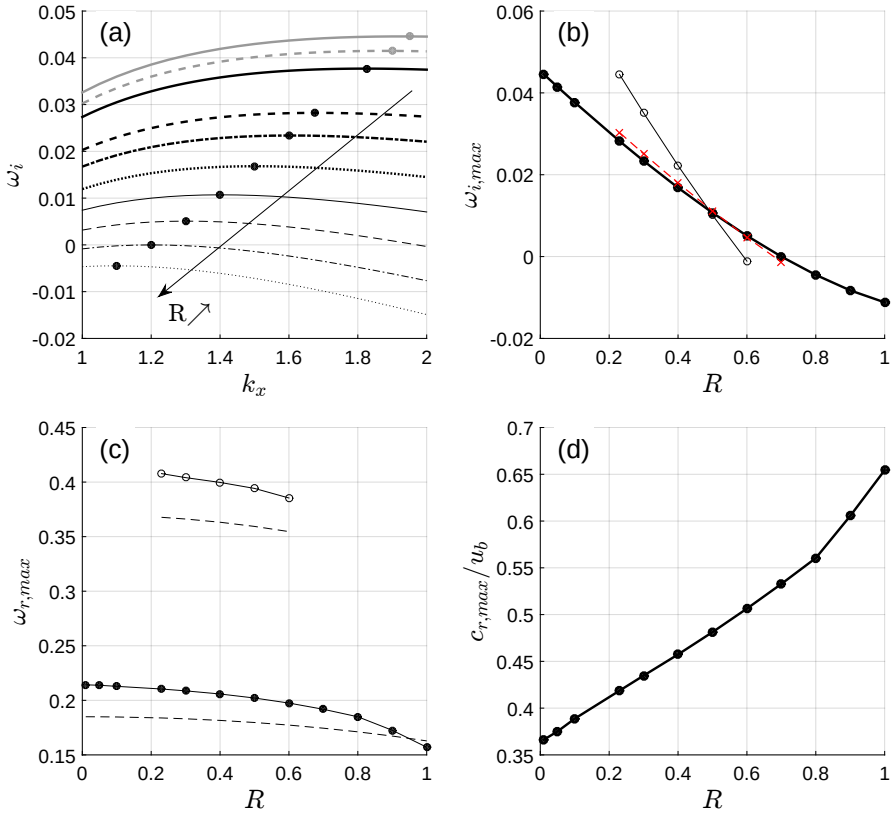

Figure 17: (a) Growth rate of the unstable mode versus wavenumber, given by a linear stability analysis of test case AC01 with several values of the resistance: —— $R = 0.01$; - - - $R = 0.05$; —— $R = 0.1$; - - - $R = 0.23$; - · - $R = 0.3$; ··· $R = 0.4$;—— $R = 0.5$; - - - $R = 0.6$; - · - $R = 0.7$; ··· $R = 0.8$. The maximum growth rate is indicated by filled symbols. (b) Maximum growth rate of the unstable mode as a function of resistance: the plain line with filled circles corresponds to case AC01, and the one with open circles to case AC02, both are obtained with the Cess velocity profile. The dashed line with × symbols corresponds to case AC01 when the stability analysis is based on the numerical velocity profile. (c) real angular frequency of the most amplified instability (filled circles for AC01; open circles for AC02; dashed lines for theoretical resonance frequencies of these MSD systems)(d) Phase speed normalized by bulk velocity as a function of resistance, for the instability having maximal growth, for baseline case AC01.

numerical simulations is not too different from the linear stability prediction, $R = 0.7$. This thus confirms the statements made in the beginning of this section.

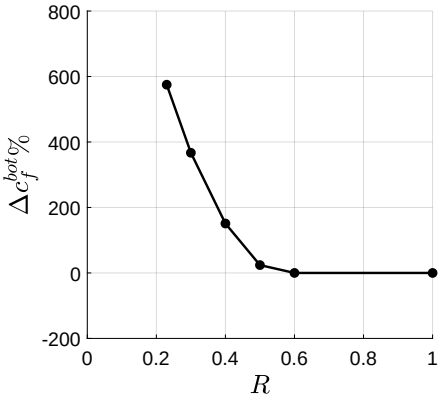

Figure 18: Drag increase at the bottom lined wall as a function of resistance, obtained in the numerical simulations by varying the resistance of baseline case AC01 (the corresponding cases are AC01, AC13, AC14, AC15, AC11, AC12).

7. Conclusion

Numerical simulations of a turbulent channel flow with an impedance boundary condition have been performed. When the liner resistance is small, and when its resonance frequency is not too large compared to a typical frequency of the flow, the turbulent statistics differ from those for a channel with rigid walls. Surface waves are also observed along the liner surface. The waves have a large wavelength compared to the turbulent structures. They modulate these structures and transport momentum toward the impedance wall, causing a drag increase. As the resonance frequency increases these waves progressively lose their spanwise coherence while their wavelength decreases to get close to the flow typical length scales, which may also results in a drag increase when the resistance is sufficiently small, as was also observed by Scalo et al. [22].

At low resonance frequencies the two-dimensional waves have a spatial distribution which resembles the waveforms observed in former experiments [5], even if the conditions differ (the simulation are periodic in the streamwise direction, the Reynolds number in the simulation is lower).

A linear two-dimensional temporal stability analysis has been performed. A temporal analysis suits the streamwise periodic configuration of the channel flow and offers a new perspective on unstable modes, compared with the more widespread spatial analysis of surface modes in acoustics. It has been shown that by tuning the resonance frequency of the liner to the frequency of a mode pertaining to the A-branch of wall modes, it is possible to destabilize this mode. Numerical simulations of a channel flow have been performed where the bottom rigid wall is suddenly replaced by an impedance wall. An instability

is then observed with characteristics similar to those obtained from a linear stability analysis. This instability saturates and leads to a final state of the flow which corresponds to a waveform different from the initial instability, but not completely different.

The liner was modeled by an impedance boundary condition corresponding to a mechanical oscillator. This has first been introduced by Tam and Auriault [6] and has been recast here to match the characteristic form of the equations used in the solver. It is a simple model that accounts for a resonance of the liner. As virtually any other impedance model, it can be derived by supposing that the incident acoustic wave has a long wavelength compared to the perforations of the face sheet. This model has been used as is in the turbulent channel numerical simulations, but some turbulent scales may be so small that the model is not valid anymore. Also it is not clear how the rugosity due to liner perforations can be accounted for by an impedance boundary condition. As a result, the low frequency waves certainly correspond to some reality (and have been observed experimentally) but the presence of small spanwise rollers at high frequency probably needs to be confirmed by experiments or simulations including the full geometry of the liner.

Ongoing work focus on spatial simulations, with a well defined inlet and outlet and no periodicity assumption. This is closer to practical situations, and also allows introducing a sound wave into the domain. The triggering of the surface wave by an incoming wave is indeed important physically. In the present paper, the periodic streamwise boundary conditions probably act as means to sustain the wave as an incoming wave would do in a spatial simulation.

Acknowledgments

This work was performed using HPC resources from GENCI-CINES (Grant A0022A07582), and from the Mésocentre SPIN Calcul of the Université of Poitiers.

Appendix A. Grid convergence study

The mesh size requirement in the vicinity of an impedance wall is not as well established as for a rigid wall. Hence, in this section we perform a grid convergence study to determine the grid requirements for accurate numerical simulations with impedance walls. The different configurations studied in this appendix are summarized in Table A.4. Four test cases from Table 1 are considered (AC01,AC02,AC03,AC05), which are those for which the impedance affect the more the flow dynamics. For AC01 and AC02, a 2D traveling surface wave is observed in the domain, which strongly interacts with the flow due to blowing and suction at the wall. Hence, we perform the grid convergence study mainly focused on refinement in the wall-normal direction. For AC03 we observe quasi-2D surface waves with ripples in the span-wise direction, therefore we study

Table A.4: Test cases for grid convergence analysis using impedance wall boundary condition.

	$L_x \times L_y \times L_z$	$\mathcal{M}$	R	ω_{res}	$N_x \times N_y \times N_z$	Δx^+	Δy^+_{min}	Δz^+	$\Delta c_f^{\text{bot}}\%$	$\Delta c_f^{\text{top}}\%$
AC01cc	$6\pi h \times 2h \times \pi h$	0.3	0.23	0.185	$351 \times 151 \times 125$	20	1	10	443	44
AC01c	$6\pi h \times 2h \times \pi h$	0.3	0.23	0.185	$351 \times 171 \times 125$	20	0.5	10	573	45
AC01	$6\pi h \times 2h \times \pi h$	0.3	0.23	0.185	$351 \times 201 \times 125$	20	0.25	10	575	44
AC02c	$3\pi h \times 2h \times \pi h$	0.3	0.23	0.367	$185 \times 151 \times 125$	20	1	10	162	20
AC02	$3\pi h \times 2h \times \pi h$	0.3	0.23	0.367	$185 \times 171 \times 125$	20	0.5	10	159	18
AC03c	$3\pi h \times 2h \times \pi h$	0.3	0.23	0.738	$185 \times 151 \times 125$	20	1	10	74	7
AC03	$3\pi h \times 2h \times \pi h$	0.3	0.23	0.738	$91 \times 151 \times 61$	40	1	20	78	-1
AC05	$3\pi h \times 2h \times \pi h$	0.3	0.23	2.960	$185 \times 151 \times 125$	20	1	10	0	-3
AC05w	$3\pi h \times 2h \times 2\pi h$	0.3	0.23	2.960	$185 \times 151 \times 251$	20	1	10	-2	-4
R0.1cc	$6h \times 2h \times 6h$	0.5	0.10	3.140	$115 \times 151 \times 251$	20	1	10	161	188
R0.1c	$6h \times 2h \times 6h$	0.5	0.10	3.140	$115 \times 171 \times 251$	20	0.5	10	176	176
R0.1	$6h \times 2h \times 6h$	0.5	0.10	3.140	$115 \times 201 \times 251$	20	0.25	10	181	181

the grid coarsening in the stream- and span-wise directions. With case AC05 we check the influence of domain size in the span-wise direction. In addition, to validate our computations against the simulations of Scalo et al. [22] (to our knowledge, the only published work for which turbulence with impedance walls has been documented), a configuration taken from this reference has been computed and is referred to as R0.1 in the table. In this configuration, the resistance R=0.1 is smaller than generally used in this work, and both top and bottom walls are impedance walls, whereas for cases AC01-AC05 only the bottom wall is an impedance wall. Also, the Mach number value is larger, $\mathcal{M}$=0.5. All in all, configuration R0.1 is not hugely different from the test case AC09, except that for the latter only the bottom wall is lined. Our domain size for test case R0.1 is the same as Scalo et al [22], and our finer grid verifies $\Delta x^+ \times \Delta y^+ \times \Delta z^+ = 20 \times 0.25 \times 10$ (with + units based on Re_τ=395). Scalo et al grid resolution is $\Delta x^{++} \times \Delta y^{++} \times \Delta z^{++} = 27.7 \times 0.6 \times 21.6$ where ++ denotes normalization by wall units of the simulation. Converted into + units based on Re_τ=395 , this gives $\Delta x^+ \times \Delta y^+ \times \Delta z^+ \sim 17.5 \times 0.37 \times 13.5$. Hence, the resolutions are comparable.

All simulations share the same value Re_b=6900. For an incompressible channel flow with rigid walls (a configuration referred to as M395 in the paper) at similar Re_b and $\mathcal{M}$ one would have Re_τ=395. For impedance walls it is not possible to estimate the friction Reynolds number *a priori*. Hence, all the grid resolution mentioned in Table A.4 are based on the value of Re_τ for a rigid wall simulation. Similarly $\Delta c_f\%$ computed for the two walls are based on the velocity and length scales computed for bottom impedance and top rigid wall separately.

Results of the grid convergence analysis are shown in Fig. A.19, where the mean stream-wise velocity, as well as the rms of stream-wise and wall-normal

velocity are presented. Results in Fig. A.19 are non-dimensionalised with

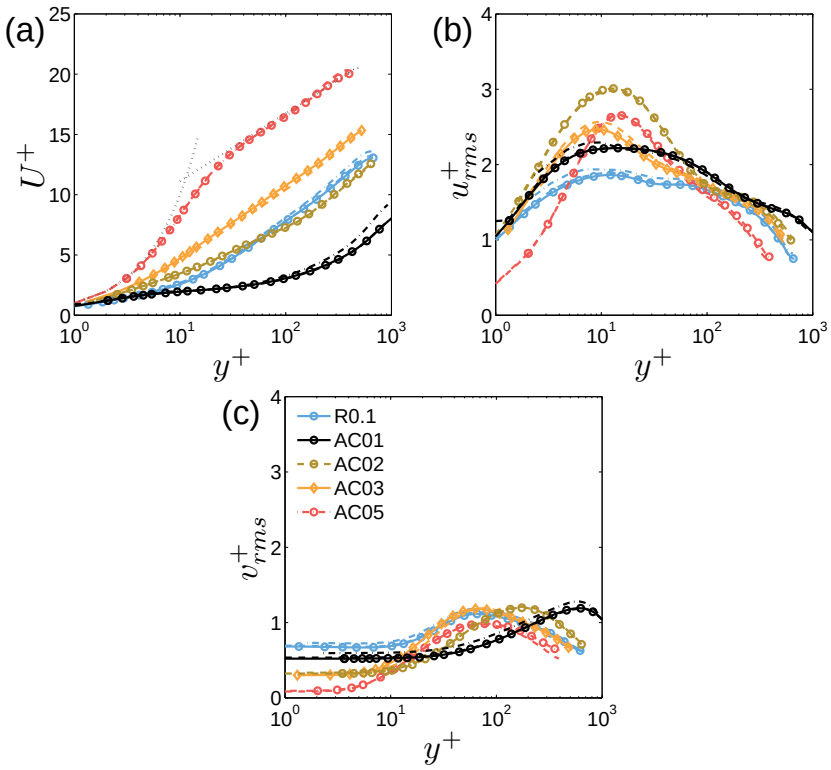

Figure A.19: Grid convergence for impedance wall test cases. In the legend only the the most well resolved cases (e. g. AC01) are indicated (line+symbols). Cases with medium resolution (e. g. AC01c) are shown by a dashed line, while cases with the worst resolution (e. g. AC01cc) are shown by a dash-dotted line, where lines are of the same color as the most well resolved case. Lines of medium and high resolution are superimposed, only the line corresponding to the worst resolution stands apart in some cases.

wall units of the bottom impedance wall. These results do not depend much on the grid resolution, which is therefore deemed to be sufficient in all test cases. From this study the grid resolution that is required in the directions parallel to the wall is Δx^+=20 and Δz^+=10 (computed with equivalent friction Reynolds number Re_τ=395 in rigid-wall simulation). In the wall-normal direction, a minimal mesh size y^+_{min}=0.25-1 is necessary. These values are about the same, or slightly more stringent than required for a rigid wall. In particular the smaller the resistance of the MSD wall the smaller y^+_{min} should be.

The profiles for the mean flow, rms of streamwise velocity, and rms of spanwise velocity for case R0.1 are compared to the ones obtained by Scalo et al. [22] for the same configuration in Fig. A.20, where the rigid wall case M395 is also shown. Although an exact agreement with the results of Scalo et al. [22] is not

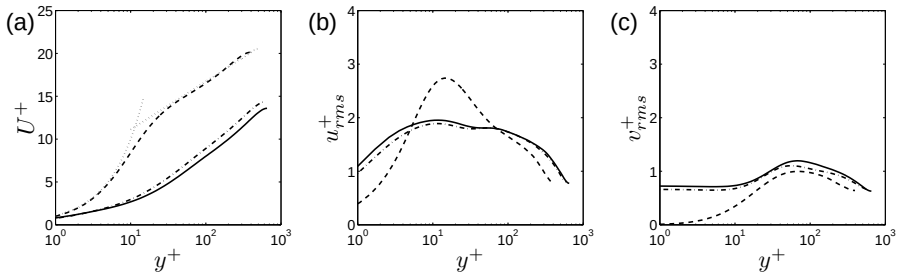

Figure A.20: Comparison between the present simulation and that from Scalo et al. [22] for case R0.1. (a) Mean velocity; (b) rms of streamwise velocity; (c) rms of wall-normal velocity. Lines are: —— presents result; - · - Scalo et al. results; - - - rigid wall case M395.

obtained (their simulation is also a large eddy simulation), both simulations provide close results. The difference seen in the mean velocity profile also shows up in the drag increase: we computed a larger drag increase (≈180%) for case R0.1, whereas Scalo et al. report a value of 148%. Nevertheless, despites these differences, it is clear that both simulations show similar changes compared to the rigid channel flow.

Appendix B. Linear stability analysis

To perform the stability analysis, the linearized two-dimensional Navier-Stokes equations are considered. For the linearization all variables are splitted as a sum of a base flow indicated by subscript 0, and a perturbation indicated with a tilde: $\rho(x,y) = \rho_0 + \tilde{\rho}(x,y,t)$; $u(x,y,t) = U_0(y) + \tilde{u}(x,y,t)$; $v(x,y,t) = \tilde{v}(x,y,t)$; $p(x,y,t) = p_0 + \tilde{p}(x,y,t)$; $T(x,y,t) = T_0 + \tilde{T}(x,y,t)$. The base flow is taken to be essentially a shear flow with a streamwise component $U_0(y)$ that depends on y. In our simulation, the Mach number is small, as a result no dependence of the base density ρ_0 and temperature T_0 upon y is considered. The linearized

equations for the perturbations are:

$$\frac{\partial\tilde{\rho}}{\partial t}+U_0\frac{\partial\tilde{\rho}}{\partial x}+\left(\frac{\partial\tilde{u}}{\partial x}+\frac{\partial\tilde{v}}{\partial y}\right)=0 \tag{B.1}$$

$$\frac{\partial\tilde{u}}{\partial t}+U_0\frac{\partial\tilde{u}}{\partial x}+\tilde{v}\frac{\mathrm{d}U_0}{\mathrm{d}y}+\frac{\partial\tilde{p}}{\partial x}=\frac{1}{\mathrm{Re}}\mu_T\Delta\tilde{u}+\frac{1}{\mathrm{Re}}\left(\frac{\mu_T}{3}+\frac{\kappa}{\mu}\right)\frac{\partial}{\partial x}\left(\frac{\partial\tilde{u}}{\partial x}+\frac{\partial\tilde{v}}{\partial y}\right)\cdots + \frac{1}{\mathrm{Re}}\frac{\mathrm{d}\mu_T}{\mathrm{d}y}\left(\frac{\partial\tilde{u}}{\partial y}+\frac{\partial\tilde{v}}{\partial x}\right) \tag{B.2}$$

$$\frac{\partial\tilde{v}}{\partial t}+U_0\frac{\partial\tilde{v}}{\partial x}+\frac{\partial\tilde{p}}{\partial y}=\frac{1}{\mathrm{Re}}\mu_T\Delta\tilde{v}+\frac{1}{\mathrm{Re}}\left(\frac{\mu_T}{3}+\frac{\kappa}{\mu}\right)\frac{\partial}{\partial y}\left(\frac{\partial\tilde{u}}{\partial x}+\frac{\partial\tilde{v}}{\partial y}\right)\cdots - \frac{2}{3}\frac{1}{\mathrm{Re}}\frac{\mathrm{d}\mu_T}{\mathrm{d}y}\frac{\partial\tilde{u}}{\partial x}+\frac{4}{3}\frac{1}{\mathrm{Re}}\frac{\mathrm{d}\mu_T}{\mathrm{d}y}\frac{\partial\tilde{v}}{\partial y} \tag{B.3}$$

$$\frac{\partial\tilde{p}}{\partial t}+U_0\frac{\partial\tilde{p}}{\partial x}+\left(\frac{\partial\tilde{u}}{\partial x}+\frac{\partial\tilde{v}}{\partial y}\right)=\frac{1}{\mathrm{RePr}}\left(1+\frac{\nu_t\mathrm{Pr}}{\gamma\mathrm{Pr_t}}\right)\Delta\tilde{T}+\frac{1}{\gamma\mathrm{RePr_t}}\frac{\mathrm{d}\nu_t}{\mathrm{d}y}\frac{\partial\tilde{T}}{\partial y}\cdots + \frac{(\gamma-1)}{\mathrm{Re}}2\frac{\mathrm{d}U_0}{\mathrm{d}y}\left(\frac{\partial\tilde{u}}{\partial y}+\frac{\partial\tilde{v}}{\partial x}\right) \tag{B.4}$$

$$\tilde{p}=\frac{1}{\gamma}(\tilde{T}+\tilde{\rho}) \tag{B.5}$$

These equations are normalized with the same reference quantities as used in the numerical solver (see Section 2.1). Since the temperature is uniform here, the speed of sound at the wall is simply the speed of sound anywhere. For completeness, a turbulent eddy viscosity $\mu_t(y)$ depending on y has been retained. The result obtained with this eddy viscosity were slightly different but neither better or worse than the ones presented in the paper which were obtained by accounting only for the molecular viscosity. The total viscosity (molecular + turbulent) is $\mu_T(y) = \mu + \mu_t(y)$. The corresponding dynamic viscosity (obtained after division by the uniform ρ_0) is $\nu_T(y) = \nu + \nu_t(y)$. For the results presented in the paper and obtained with the sole molecular viscosity, one has: $\mu_t(y)$=0, $\nu_t(y) = 0$, $\nu_T(y) = \nu$.

For a temporal stability analysis, modal solutions of the form $\tilde{u}(y) = \hat{u}(y)\mathrm{e}^{\mathrm{i}(k_x x-\omega t)}$ are searched for, where k_x is a real wavenumber and ω is the complex angular frequency. Injecting this solution into Eqs. (B.1-B.5), discretizing these equations on a y-grid and denoting by $\mathbf{D}$ the corresponding derivation matrix [25] provides the generalized eigenvalue problem:

$$(\mathbf{A}+\omega\mathbf{B})\,\mathbf{\Psi}=0 \tag{B.6}$$

where:

$$\mathbf{A}=\left[\begin{array}{c|c|c|c|c} \mathrm{i}k_x\mathbf{U_0} & \mathrm{i}k_x\mathbf{I} & \mathbf{D} & & \\ \hline & \mathrm{i}k_x\mathbf{U_0}+\mathbf{A}_1 & \mathbf{U_0'}+\mathbf{A}_2 & & \\ \hline & \mathbf{A}_3 & \mathrm{i}k_x\mathbf{U_0}+\mathbf{A}_4 & \mathbf{D} & \\ \hline & \mathrm{i}k_x\mathbf{I}+\mathbf{A}_5 & \mathbf{D}+\mathbf{A}_6 & \mathrm{i}k_x\mathbf{U_0} & \mathbf{A}_7 \\ \hline -\frac{1}{\gamma}\mathbf{I} & & & \mathbf{I} & -\frac{1}{\gamma}\mathbf{I} \end{array}\right] \tag{B.7}$$

$$\mathbf{B} = \left[\begin{array}{c|c|c|c|c} -\mathrm{i}\mathbf{I} & & & & \\ \hline & -\mathrm{i}\mathbf{I} & & & \\ \hline & & -\mathrm{i}\mathbf{I} & & \\ \hline & & & -\mathrm{i}\mathbf{I} & \\ \hline & & & & \end{array}\right] \tag{B.8}$$

$$\mathbf{A}_1 = \frac{1}{\mathrm{Re}}\left(\frac{4}{3}\mathbf{N_T} + \mathbf{K}\right)k_x^2 - \frac{1}{\mathrm{Re}}(\mathbf{N_T}\mathbf{D}^2 + \mathbf{N'_T}\mathbf{D}) \tag{B.9}$$

$$\mathbf{A}_2 = -\frac{1}{\mathrm{Re}}\left(\frac{1}{3}\mathbf{N_T} + \mathbf{K}\right)\mathrm{i}k_x\mathbf{D} - \frac{\mathrm{i}k_x}{\mathrm{Re}}\mathbf{N'_T} \tag{B.10}$$

$$\mathbf{A}_3 = -\frac{1}{\mathrm{Re}}\left(\frac{1}{3}\mathbf{N_T} + \mathbf{K}\right)\mathrm{i}k_x\mathbf{D} + \frac{2}{3\mathrm{Re}}\mathrm{i}k_x\mathbf{N'_T} \tag{B.11}$$

$$\mathbf{A}_4 = -\frac{1}{\mathrm{Re}}\left(\frac{4}{3}\mathbf{N_T} + \mathbf{K}\right)\mathbf{D}^2 + \frac{1}{\mathrm{Re}}\left(k_x^2\mathbf{N_T} - \frac{4}{3}\mathbf{N'_T}\mathbf{D}\right) \tag{B.12}$$

$$\mathbf{A}_5 = -\frac{2(\gamma-1)}{\mathrm{Re}}\mathbf{U'_0}\mathbf{D} \tag{B.13}$$

$$\mathbf{A}_6 = -\frac{2(\gamma-1)}{\mathrm{Re}}\mathrm{i}k_x\mathbf{U'_0} \tag{B.14}$$

$$\mathbf{A}_7 = \frac{1}{\mathrm{RePr}}\left(\mathbf{I} + \frac{\mathrm{Pr}}{\gamma\mathrm{Pr_t}}\mathbf{N_t}\right)(k_x^2\mathbf{I} - \mathbf{D}^2) - \frac{1}{\gamma\mathrm{RePr_t}}\mathbf{N'_t}\mathbf{D} \tag{B.15}$$

The vector of unknown is $\mathbf{\Psi} = [\mathbf{R}\ \mathbf{U}\ \mathbf{V}\ \mathbf{P}\ \mathbf{T}]^t$ where $\mathbf{U}$ for example contains the values of $\hat{u}$ at the grid points.
$\mathbf{U_0}$ and $\mathbf{U'_0}$ are matrices containing the velocity and velocity derivative at the grid points. $\mathbf{N_T}$ is the square matrix containing the total viscosity (ν_T) at the grid points in its diagonal; $\mathbf{N'_T}$ is the square matrix containing the y-derivative of the total viscosity ($\mathrm{d}\nu_T/\mathrm{d}y$) in its diagonal; $\mathbf{N_t}$ is the square matrix with the turbulent eddy viscosity only (ν_t) in its diagonal; $\mathbf{N'_t}$ is the square matrix with the y-derivative of the turbulent eddy viscosity only ($\mathrm{d}\nu_t/\mathrm{d}y$) in its diagonal.

Finally, the implementation of the impedance boundary condition is discussed. Contrary to the spatial stability case, in the general case when the impedance $Z(\omega)$ is a transcendental function of ω it would not be possible to easily insert the impedance boundary condition into Eq. (B.6). As the present MSD boundary condition leads to an algebraic function of ω, there is no such difficulty. Taking the Fourier transform of Eqs. (18-19), one obtains:

$$\tilde{q} + \quad \omega \quad (\mathrm{i}\tilde{v}) = 0 \qquad (\text{ at } y = -1) \tag{B.16}$$

$$K\tilde{v} + \quad \omega \quad (-\mathrm{i}M\tilde{q} - \mathrm{i}R\tilde{v} - \mathrm{i}\tilde{p}) = 0 \qquad (\text{ at } y = -1) \tag{B.17}$$

To introduce this into Eq. (B.6), one has to add one unknown $\tilde{q}$ in the vector $\mathbf{\Psi}$, and add an extra line in Eq. (B.6) that corresponds to the first equation, Eq. (B.16), in the former system. The second equation of the system, Eq. (B.17), replaces the equation for $\tilde{v}$ at the bottom wall in Eq. (B.6). Overall the matrices $\mathbf{A}$ and $\mathbf{B}$ are square of size $(5N{+}6)\mathrm{x}(5N{+}6)$, where N is the number of discretization points in the y-direction.

References

References

[1] A. W. Guess, Calculation of perforated plate liner parameters from specified acoustic resistance and reactance, J. Sound Vib. 40(1) (1975) 119–137.

[2] A. L. Goldman, R. Panton, Measurement of the acoustic impedance of an orifice under a turbulent boundary layer, J. Acoust. Soc. Am. 60(6) (1976) 1397–1404.

[3] X. Jing, X. Sun, J. Wu, K. Meng, Effect of grazing flow on the acoustic impedance of an orifice, AIAA J. 39(8) (2001) 1478–1484.

[4] J. D. Wolter, Drag measurements of porous plate acoustic liners, NASA/TM - report 2005-213570, 2005.

[5] D. Marx, Y. Aurégan, H. Bailliet, J.-C. Valière, PIV and LDV evidence of hydrodynamic instability over a liner in a duct with flow, J. Sound Vib. 329 (2010) 3798-3812.

[6] C. K. W. Tam, L. Auriault, Time-Domain Impedance Boundary Conditions for Computational Aeroacoustics, AIAA J. 34(5) (1996) 917-923. doi: 10.2514/3.13168

[7] Y. Ozyoruk, L. N. Long, M. G. Jones, Time-domain numerical simulation of a flow-impedance tube, J. Comput. Phys. 146 (1998) 29–57. doi: 10.1006/jcph.1998.5919

[8] Y. Ozyoruk, L. N. Long, Time-domain calculation of sound propagation in lined ducts with sheared flows, AIAA J. 39(5) (2000) 768–773. doi: 10.2514/2.1056

[9] S. Zheng, M. Zhuang, Three-Dimensional Benchmark Problem for Broadband Time-Domain Impedance Boundary Conditions, AIAA J. 42 (2) (2004) 405-407.

[10] S. Rienstra, Impedance models in time domain, including the extended Helmholtz resonator model, 12th AIAA/CEAS Aeroacoustics Conference, AIAA Paper 2006-2686, 2006. doi: 10.2514/6.2006-2686

[11] X. Li, C. Richter, F. Thiele, Time-domain impedance boundary conditions for surfaces with subsonic mean flows, J. Acoust. Soc. Am., 119(5) (2006) 2665–2676. doi: 10.1121/1.2191610

[12] C. Richter, F. H. Thiele, X. Li, M. Zhuang, Comparison of time-domain impedance boundary conditions for lined duct flows, AIAA J. 45(6) (2007) 1333–1345. doi: 10.2514/1.24945

[13] G. Gabard, E. Brambley, A full discrete dispersion analysis of time-domain simulations of acoustic liners with flow, J. Comput. Phys. 273 (2014) 310–326. doi: 10.1016/j.jcp.2014.05.004

[14] D. Marx, Numerical Computation of a lined duct instability using the linearized Euler equations, AIAA J. 53 (8) (2015) 2379-2388.

[15] E. J. Brambley, G. Gabard, Time-domain implementation of an impedance boundary condition with boundary layer correction, J. Comput. Phys. 321 (2016) 755-775.

[16] B. Xin, D. Sun, X. Jing, X. Sun, Numerical study of acoustic instability in a partly lined flow duct using the full linearized Navier-Stokes equations, J. Sound Vib. 373 (2016) 132–146. doi: 10.1016/j.jsv.2016.02.042

[17] C. K. W. Tam, K. A. Kurbastkii, K. K. Ahuja, R. J. Gaeta, A numerical and experimental investigation of the dissipation mechanisms of resonant acoustic liners, J. Sound Vib. 245 (2001) 545–557.

[18] C. K. W. Tam, H. Ju, B. E. Walker, Numerical Simulation of a Slit Resonator in a Grazing Flow Under Acoustic Excitation, J. Sound Vib. 313 (2008) 449–471.

[19] Q. Zhang, D. J. Bodony, Numerical simulation of two-dimensional acoustic liners with high-speed grazing flows, AIAA J. 49(2) (2011) 365–382.

[20] Q. Zhang, D. J. Bodony, Numerical investigation and modelling of acoustically excited flow through a circular orifice backed by a hexagonal cavity, J. Fluid Mech. 693 (2012) 367–401.

[21] S. Olivetti, R. D. Sandberg, B. J.Tester, Direct numerical simulation of turbulent flow with an impedance condition, J. Sound Vib. 344 (2015) 28–37.

[22] C. Scalo, J. Bodart, S. Lele, Compressible turbulent channel flow with impedance boundary conditions, Phys. Fluids 27 (2015) 035107.

[23] J. Jimenez, M. Uhlmann, A. Pinelli, G. Kawahara, Turbulent shear flow over active and passive porous surfaces, J. Fluid Mech. 442 (2001) 89-117.

[24] D. Marx, Y. Aurégan, Comparison of experiments with stability analysis predictions in a lined flow duct, Proceedings of the 16th AIAA/CEAS Aeroacoustics Conference, AIAA Aviation Forum, 5-9 june 2010, Stockholm, AIAA Paper AIAA 2010-3946.

[25] D. Marx, Y. Aurégan, Effect of turbulent eddy viscosity on the unstable surface mode above an acoustic liner, J. Sound Vib. 332(15) (2013) 3803–3820. doi: 10.1016/j.jsv.2013.02.005

[26] B. Y. Zhou, N. R. Gauger, S. R. Koh, M. Meinke, W. Schroder, Adjoint-based trailing-edge noise minimization using porous material, 20th AIAA/CEAS aeroacoustics conference, 16-20 june 2014, Atlanta. AIAA paper 2014-3040.

[27] J. Sesterhenn, A characteristic-type formulation of the Navier-Stokes equations for high order upwind schemes, Computers and Fluids 30 (2001) 37-67.

[28] R. Lechner, J. Sesterhenn, R. Friedrich, Turbulent supersonic channel flow, J. of turbulence 2 (2001) 001.

[29] G. Coleman, J. Kim, R. Moser, A numerical study of turbulent supersonic isothermal-wall channel flow, J. Fluid Mech. 305 (1995) 159-183.

[30] N. A. Adams, K. Shariff, A high-resolution hybrid compact-ENO scheme for shock–turbulence interaction problems, J. Comput. Phys. 127 (1996) 27–51.

[31] S. K. Lele, Compact finite difference schemes with spectral-like resolution, J. Comput. Phys. 103 (1992) 16-42.

[32] E. Lamballais, V. Fortuné, S. Laizet, Straightforward high-order numerical dissipation via the viscous term for direct and large eddy simulation, J. Comput. Phys. 230 (2011) 3270-3275.

[33] T. Dairay, V. Fortuné, E. Lamballais, L. E. Brizzi, LES of a turbulent jet impinging on a heated wall using high-order numerical schemes, Int. J. Heat and Fluid Flow 50 (2014) 117–187.

[34] T. Dairay, E. Lamballais, S. Laizet, J. C. Vassilicos, Numerical dissipation vs. subgrid-scale modelling for large eddy simulation, J. Comput. Phys. 337 (2017) 252–274.

[35] R. Sebastian, D. Marx, V. Fortuné, E. Lamballais, Numerical simulation of a compressible channel flow with an acoustic liner, *Proceedings of the 23rd AIAA/CEAS Aeroacoustics Conference, AIAA Aviation Forum, 5-9 june 2017, Denver, Colorado*, AIAA Paper 2017-4034.

[36] K. Y. Fung, H. Ju, Broadband time-domain impedance models, AIAA J. 39 (2001) 1449–1454.

[37] K. Y. Fung, H. Ju, Impedance and its time-domain extensions, AIAA J. 38 (2000) 30–38.

[38] Y. Reymen, M. Baelmans, W. Desmet, Efficient implementation of Tam and Auriault's time-domain impedance boundary condition, AIAA J. 46 (2008) 2368–2376.
doi: 10.2514/1.35876

[39] B. Cotté, Ph. Blanc-Benon, C. Bogey, F. Poisson, Time-domain impedance boundary conditions for simulations of outdoor sound propagation, AIAA J. 47 (2009) 2391–2403.

[40] Y. Reymen, M. Baelmans, W. Desmet, Time-domain impedance formulation suited for broadband simulations, Proceedings of the 13rd AIAA/CEAS Aeroacoustics Conference, 2007, AIAA Paper 2007–3519.

[41] D. Dragna, P. Pineau, Ph. Blanc-Benon, A generalized recursive convolution method for time-domain propagation in porous media, J. Acoust. Soc. Am. 138 (2015) 1030–1042.

[42] Q. Douasbin, C. Scalo, L. Selle, T. Poinsot, Delayed-time domain impedance boundary conditions (D-TDIBC), J. Comput. Phys. 371 (2018) 50–66.

[43] B. Gustafsson, The convergence rate for difference approximations to mixed initial boundary value problems, Mathematics of computation 29 (1975) 396–406.

[44] J. Lin, C. Scalo, L. Hesselink, High-fidelity simulation of a standing-wave thermoacoustic-piezoelectric engine, J. Fluid Mech. 808 (2016) 19–60.

[45] D. Marx, A piecewise linear mean flow model for studying stability in a lined channel, J. Sound Vib. 331 (16) (2012) 3809–3823.

[46] Moser, R. D., Kim, J. and Mansour, N. N., Direct numerical simulation of turbulent channel flow up to Re_τ= 590, Phys. Fluids 11(4) (1999) 943-945.

[47] W. C. Reynolds, A. K. M. F. Hussain, The mechanics of an organized wave in turbulent shear flow. Part 3. Theoretical models and comparisons with experiments, J. Fluid Mech. 54 (1972) 263–288.

[48] K. Fukagata, K. Iwamoto, N. Kasagi, Contribution of Reynolds stress distribution to the skin friction in wall-bounded flows, Phys. Fluids, 14(11) (2002) L73-L76.

[49] H. Mamori, K. Fukagata, Drag reduction effect by a wave-like wall-normal body force in a turbulent channel flow, Phys. Fluids, 26(11) (2014) 115104.

[50] J. Hœpffner, K. Fukagata, Pumping or drag reduction?, J. Fluid Mech. 635 (2009) 117-187.

[51] S. W. Rienstra, A classification of duct modes based on surface waves, Wave motion 37 (2003) 119-135.
doi:10.1016/S0165-2125(02)00052-5

[52] E. J. Brambley, N. Peake, Classification of aeroacoustically relevant surface modes in cylindrical lined ducts, Wave motion 43 (2006) 301-310.
doi: 10.1016/j.wavemoti.2006.01.001

[53] S. W. Rienstra, M. Darau, Mean flow boundary layer effects of hydrodynamic instability of impedance wall, IUTAM Symposium on Computational Aero-Acoustics for aircraft noise prediction, Procedia engineering 6 (2010) 124–132.
doi: 10.1016/j.proeng.2010.09.014

[54] G. Boyer, E. Piot, J.-P. Brazier, Theoretical investigation of hydrodynamic surface mode in a lined duct with sheared flow and comparison with experiments, J. Sound Vib. 330 (2011) 1793-1809.
doi: 10.1016/j.jsv.2010.10.035

[55] N. Tilton, L. Cortelezzi, Linear stability analysis of pressure-driven flows in channels with porous walls, J. Fluid Mech. 604 (2008) 411–445.
doi:10.1017/S0022112008001341

[56] L. Pascal, E. Piot, G. Casalis, Global linear stability analysis of flow in a lined duct, J. Sound Vib. 410 (2017) 19–34.
doi:10.1016/j.jsv.2017.08.007

[57] I. Rahbari, C. Scalo, Linear Stability Analysis of Compressible Channel Flow over Porous Walls, Whither Turbulence and Big Data in the 21st Century, p. 451-467, Springer, 2017.

[58] I. Rahbari, C. Scalo, Quasi spectral bi-global stability analysis of compressible channel flow over complex impedance walls, 55th AIAA Aerospace Sciences Meeting, 2017. AIAA Paper 2017-1879.

[59] P. J. Schmid, D. S. Henningson, Stability and transition in shear flows, Springer, New York, 2000.

[60] P. M. Morse, K. U. Ingard, Theoretical acoustics, McGrawHill, New York 1968, chapter 2.3.